

Sparsity/Undersampling Tradeoffs in Anisotropic Undersampling, with Applications in MR Imaging/Spectroscopy

Hatef Monajemi*, David L. Donoho*

March 16, 2018

Abstract

We study *anisotropic* undersampling schemes like those used in multi-dimensional NMR spectroscopy and MR imaging, which sample exhaustively in certain time dimensions and randomly in others.

Our analysis shows that anisotropic undersampling schemes are equivalent to certain block-diagonal measurement systems. We develop novel exact formulas for the sparsity/undersampling tradeoffs in such measurement systems, assuming uniform sparsity fractions in each column. Our formulas predict finite- N phase transition behavior differing substantially from the well-known asymptotic phase transitions for classical Gaussian undersampling. Extensive empirical work shows that our formulas accurately describe observed finite- N behavior, while the usual formulas based on universality are substantially inaccurate at the moderate N involved in realistic applications.

We also vary the anisotropy, keeping the total number of samples fixed, and for each variation we determine the precise sparsity/undersampling tradeoff (phase transition). We show that, other things being equal, the ability to recover a sparse object decreases with an increasing number of exhaustively sampled dimensions.

keywords: Sparse Recovery, Compressed Sensing, Block Diagonal Measurement Matrix.¹

1 Introduction

1.1 Background

In Compressed Sensing (CS), one wishes to reconstruct an N -dimensional discrete signal x_0 using $n < N$ measurements. Theory shows that if x_0 is sufficiently sparse, and the $n \times N$ sensing matrix W is an *i.i.d* Gaussian random matrix, then x_0 can be reconstructed accurately and reliably from measurements $y = Wx_0$ using convex optimization; see many papers and books, such as [7, 4, 8, 30, 16, 26, 47, 3].

In general, at a given fixed level of undersampling, the chance of successful recovery depends on the sparsity of the underlying object, in an almost-binary fashion. Namely, suppose that the object x_0 is k -sparse—has at most k nonzero entries—and consider the situation where $k \sim \epsilon N$ and $n \sim \delta N$. Then, as a function of undersampling fraction $\delta = n/N$, there is, asymptotically for large N a definite interval for the sparsity fraction $\epsilon = k/N$ that permits successful recovery, while outside this range, recovery is unsuccessful.

Figure 1 depicts the situation for Gaussian measurement matrices W . It shows a so-called phase diagram $(\epsilon, \delta) \in (0, 1)^2$ and a curve $\epsilon_{\text{asy}}^*(\delta)$ separating a ‘success’ phase from a ‘failure’ phase. Namely, if $\epsilon < \epsilon_{\text{asy}}^*(\delta)$, then, with overwhelming probability for large N , convex optimization will recover x_0 exactly; while on the other hand, if $\epsilon > \epsilon_{\text{asy}}^*(\delta)$, then, with overwhelming probability, convex optimization will fail.

Exact expressions for the boundary $\epsilon_{\text{asy}}^*(\delta)$ separating success from failure were derived in [6, 11] assuming the measurement matrix is Gaussian and the problem size N is large. In [12, 14] those same expressions were experimentally observed to also describe accurately many non-Gaussian random measurement schemes. Thorough mathematical analysis now fully supports all these findings across very large classes of random matrices [2, 40].

*Department of Statistics, Stanford University, Stanford, CA

¹It is a pleasure to acknowledge discussions with the pioneers of anisotropic undersampling: Jeffrey Hoch and Adam Schuyler (U. Conn. Health Sciences), Michael Lustig (UC Berkeley), John Pauly (Stanford). This research was partially supported by NSF-DMS 1418362 and NSF-DMS 1407813. We would also like to thank the Stanford Research Computing Center for providing computational resources and support that were essential to these research results. Thanks also to the anonymous referees for many thoughtful comments.

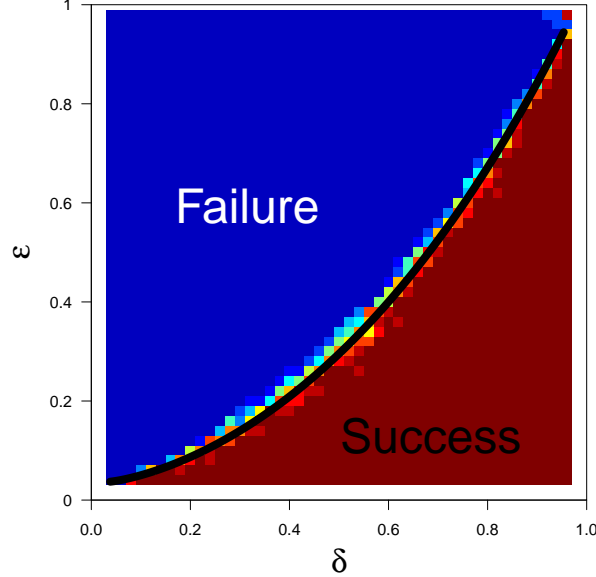


Figure 1: Success and failure regions for ‘classical’ compressed sensing with Gaussian measurement matrices; assumes object to recover is sparse and nonnegative. The asymptotic phase transition curve $\epsilon_{\text{asy}}^*(\delta)$ (solid black line) separates the two regions. Shaded attribute gives fraction of successful reconstructions. Red, 100%; blue, 0%. In this experiment, $n = 250$.

The same boundary $\epsilon_{\text{asy}}^*(\delta)$ even applies to an important class of non-random measurement matrices, see [39], so the ‘universality’ of the compressed sensing phase transition is quite broad.

As an important example, consider Fourier undersampling in a stylized model of 2-dimensional imaging. The underlying object is a two-dimensional array $x_0 = (x_0(t_0, t_1), 0 \leq t_i < M)$, whose two-dimensional discrete Fourier transform $\hat{x}_0 = \mathcal{F}_2(x_0)$ is also an M by M array ($\hat{x}_0(k_0, k_1), 0 \leq k_i < M$). The traditional experiment gathers the *fully-sampled* array $\hat{x} = (\hat{x}_0(k_0, k_1), 0 \leq k_i < M)$, systematically evaluating the 2D Fourier transform at each distinct 2D frequency index (k_0, k_1) in the range $0 \leq k_i < M$.

A *randomly-undersampled k -space experiment* first selects n distinct pairs $(k_{0,i}, k_{1,i})$ uniformly at random from among all such pairs, and then evaluates the Fourier transform just at those $n < N = M^2$ points. Letting $\mathcal{K}_2 = \{(k_{0,i}, k_{1,i}), i = 1, \dots, n\}$ denote the list of sampled k -space pairs, the undersampled Fourier transform operator $\mathcal{F}_{\text{US}} \equiv \mathcal{F}_{\text{US}}(\cdot; \mathcal{K}_2)$ produces as output $\mathcal{F}_{\text{US}}(x_0) = (\hat{x}_0(k_{0,i}, k_{1,i}), i = 1, \dots, n)$. Mimicking the Gaussian measurements case, one attempts to reconstruct by ℓ_1 minimization:

$$(P_1^{\text{US}}) \quad \arg \min_x \|x\|_1 \quad \text{subject to} \quad \mathcal{F}_{\text{US}}(x) = \mathcal{F}_{\text{US}}(x_0).$$

Depending on the details of the sampling schedule $(k_{0,i}, k_{1,i})$ and the sparsity level in x_0 , this strategy might be successful or unsuccessful. The random undersampling situation has been studied carefully empirically, and a phase transition from success to failure for this sampling scheme has been observed [13, 39], and shown to agree with the phase transition curve for Gaussian measurements. So we observe another instance of the ‘universality’ of Figure 1. However, clearly not *every* measurement scheme can behave equivalently to Gaussian measurements,

1.2 Anisotropic Undersampling

This paper studies an important class of anisotropic undersampling schemes that exhibit novel theoretical behavior and arise naturally in MR imaging and NMR spectroscopy.

Let’s give a concrete example of anisotropic undersampling. As earlier, the underlying object is a 2D $M \times M$ array x_0 with \hat{x}_0 a full $M \times M$ array of potential Fourier measurements. We undersample anisotropically by randomly selecting $m < M$ rows of the array, and then sampling *everything* within each selected row, producing $n = m \cdot M$ samples overall. We implement this concretely by sampling uniformly at random m distinct integers $k_{1,i}$ from the set $0 \leq k_1 < M$, forming a list \mathcal{K}_1 of m row indices (See Figure 3). The operator $\mathcal{F}_{\text{AUS}} = \mathcal{F}_{\text{AUS}}(\cdot; \mathcal{K}_1)$ yields the

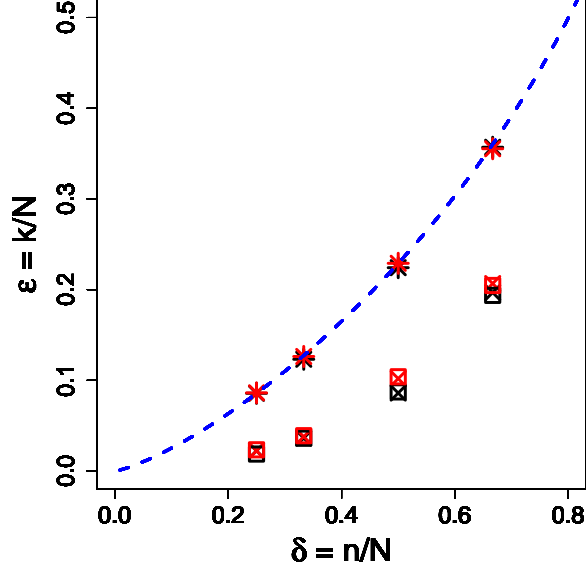


Figure 2: Observed Finite- N phase transitions for anisotropic undersampling and for block diagonal measurements studied in this paper. The \times symbol indicates finite- N phase transition for anisotropic undersampling experiments using partial 2D FT where a specific fraction δ of rows are selected uniformly at random, and then each selected row is sampled exhaustively. The $*$ symbol indicates isotropic undersampling experiments using a partial 2D FT where a certain fraction of k -space samples are selected uniformly at random. The \square symbol indicates experimental data from a block diagonal measurement matrix with a single repeated Gaussian random matrix block. The colors indicate different problem sizes. Black stands for a 24×24 grid and red for a 48×48 grid. The dashed blue line gives the asymptotic phase transition location for complex-valued Gaussian measurement ensembles. The isotropic undersampling data lie close to the dashed blue line, while the anisotropic undersampling data are substantially displaced.

partial measurements $\mathcal{F}_{\text{AUS}}(x_0) \equiv (\hat{x}_0(k_0, k_{1,i}), i = 1, \dots, m, 0 \leq k_0 < M)$. No other samples are collected. The subscript AUS reminds us of the anisotropic undersampling². Again assuming sparsity of the object to be recovered, attempt to reconstruct using ℓ_1 minimization:

$$(P_1^{\text{AUS}}) \quad \arg \min_x \|x\|_1 \quad \text{subject to} \quad \mathcal{F}_{\text{AUS}}(x) = \mathcal{F}_{\text{AUS}}(x_0).$$

Once again, one can observe experimentally that the sparsity level determines success or failure.

Figure 2 shows results from an empirical study of the sparsity-undersampling tradeoff for anisotropic undersampling. It displays the location of the empirical phase transition from success to failure for our reconstruction from anisotropic undersampling, as a function of underlying sparsity fraction ϵ ; when the object's sparsity fraction $\epsilon = k/N$ falls below the depicted transition point, success is the predicted outcome, whereas when the object sparsity fraction ϵ exceeds that level, we predict failure.

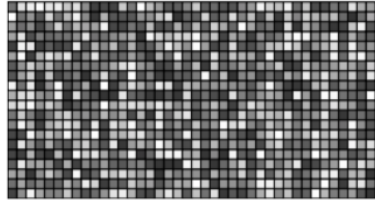
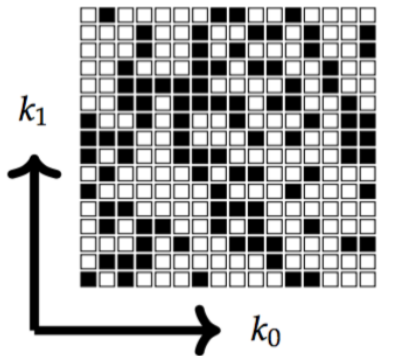
Let's call the earlier random- k -space undersampling scheme *isotropic*. The terminology reminds us that for isotropic sampling, k_0 and k_1 are scattered randomly with no directional preference, while for anisotropic sampling, the sampling scheme is exhaustive in the k_0 coordinate and random in k_1 as depicted schematically in Figure 3. Empirical phase transitions for the isotropic sampling scheme are also shown in Figure 2.

The striking comparison is that, while there are definite phase transitions in each case, the anisotropic ones don't occur at the same place as the isotropic ones; instead the transitions for the anisotropic sampling are shifted downwards substantially from the phase transitions for the isotropic scheme. Formulas for the precise amount of shift are presented below.³

² Under the notation we are using, anisotropic undersampling could also be represented using the general undersampling operator - $\mathcal{F}_{\text{AUS}}(\cdot; \mathcal{K}_1) \equiv \mathcal{F}_{\text{US}}(\cdot; \{0, \dots, M-1\} \times \mathcal{K}_1)$ - however it simplifies discussion to have a dedicated notation.

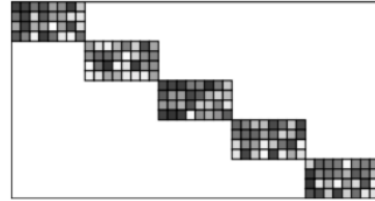
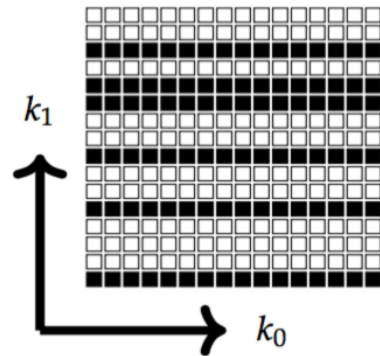
³It will still be the case that at sufficiently large N , the shift goes away; however, it will become clear that the required N are unreasonably large, so such schemes in practice will always exhibit a noticeable shift, by an amount we here quantify precisely.

Isotropic Undersampling



Dense Measurement Matrix

Anisotropic Undersampling



BD Measurement Matrix

Figure 3: Emblems of isotropic (upper left) and anisotropic (upper right) k -space undersampling discussed in this paper. Traditional compressed sensing literature studies isotropic k -space undersampling, whereas anisotropic undersampling is similar to practical schemes commonly used in MR imaging/spectroscopy. Lower left panel depicts a dense measurement matrix of the type produced by isotropic k -space undersampling, while lower right panel depicts a block diagonal measurement matrix associated to anisotropic k -space undersampling. The k -space sampling plans of the top row are equivalent under an appropriate isometry to undersampling matrices depicted in the bottom row. The figure serves merely as a ‘cartoon illustration’ of the concept of equivalence established in this paper and so the size and number of blocks should not be taken literally.

Figure 2 also shows a curve giving the location of the phase transition in the Gaussian case with comparable sparsity and n and N . This curve goes quite near the empirical phase transitions for isotropic sampling, confirming the results of [13, 39]. Consequently, we can also say that the anisotropic undersampling results differ substantially from the Gaussian undersampling results.

1.3 Block Diagonal Undersampling

Figure 2 actually displays empirical results for *three* seemingly very different situations. The first two were mentioned: isotropic and anisotropic undersampling in 2D Fourier imaging, respectively.

The third situation is seemingly unrelated to 2D Fourier imaging: *block-diagonal Gaussian undersampling*. In that setting, the object is a 1D vector of length M^2 , partitioned into M blocks of size M each. For a given undersampling parameter $m < M$, the measurement matrix A is $n = m \cdot M$ by $N = M \cdot M$, and has a block-diagonal form made of M blocks, each of size m by M . The off-diagonal blocks are all zero, and the diagonal blocks are random, filled with i.i.d. Gaussian entries. The object to recover \mathbf{x}_0 is a sparse vector of length $N = M^2$. The measurements are $\mathbf{y} = A\mathbf{x}_0$.

Figure 2 shows the the finite- N phase transitions of block-diagonal undersampling schemes, but they are hard to discern; the locations are visually quite close to those of anisotropic undersampling, given the same values for the

underlying undersampling fraction $\delta = n/N$ and sparsity k/N .

1.4 This paper’s contribution

This paper shows that the observed equality of phase transition between anisotropic undersampling and block-diagonal undersampling is no coincidence. It demonstrates the formal theoretical equivalence of anisotropic undersampling with appropriate block-diagonal undersampling. It then exploits this equivalence, by deriving precise formulas for the finite- N phase transitions of sparse reconstruction from block-diagonal undersampling. These formulas are rigorously proven in one class of situations, but the formulas arising from our study are shown empirically to accurately predict phase transitions observed in anisotropic undersampling in Figure 2 and several other situations.

We have so far presented just the example of anisotropic undersampling in 2D Fourier imaging, but this is only a special case of our general results, which apply to fully general anisotropic undersampling of d -dimensional Fourier imaging, in which some dimensions are sampled uniformly at random and others are sampled exhaustively. In dimension $d = 2$ there is only one type of anisotropic sampling; but in higher dimensions one can have d_r dimensions sampled randomly and d_e dimensions sampled exhaustively, covering all $d = d_r + d_e$ dimensions. The case described so far is simply $d_r = 1, d_e = 1, d = 2$; but our results and methods are far more general.

An important conclusion from our study – see Corollary 8.1 – will be that, for a given number n of observations, the best sparsity-undersampling tradeoffs are obtained when d_e is as small as possible and d_r is as large as possible, in a way that we can quantify precisely. While that would seem to suggest always using $d_e = 0$ and hence using isotropic undersampling, in certain applications, randomness can only be implemented in a subset of the dimensions.

1.5 Application Areas

Our results have stylized applications to two important practical fields: MR imaging and NMR spectroscopy. In either setting, the experiment produces a sequence of *free induction decays* (FIDs); these are individual time series output by radio-frequency receivers. They are variously called repetitions, interleaves, or phase-encodes in MRI. In such a sequence the acquired data may be labeled $(k_0; k_1, \dots, k_{d-1})$, with k_0 indexing the time samples of the FID and (k_1, \dots, k_{d-1}) indexing the FID itself. Under complete acquisition, we would acquire a complete collection of FID’s, and thereby obtain a complete Cartesian sampling spanning $0 \leq k_i < M, i = 0, \dots, d - 1$, while under anisotropic undersampling, we would acquire only a subset of FID’s. In more detail:

- *Multi-dimensional MR imaging.* Ordinary MR imaging, producing a single 2D image, is effectively a case of $d = 2$ -dimensional Fourier imaging. Higher-dimensional MR imaging can be either 3D (x, y, z) or dynamic (t, x, y) or 3D dynamic (t, x, y, z) .

In MR imaging experiments, each FID $(\hat{x}(k_0, \dots, k_{d-1}), 0 \leq k_0 < M)$ can be viewed as the sequence of samples of the traditional complex-valued d -dimensional Fourier transform along an axis-oriented line $u \mapsto (u, k_1, \dots, k_{d-1})$ for $u = 0, 1, \dots, M - 1$ in the d -dimensional data hypercube.

Anisotropic undersampling has been used in some way in MRI for many years in some cases for the purpose of accelerating image acquisitions [29, 33, 32, 44, 41, 31, 24]. It has been called ‘random undersampling in the indirect dimensions or ‘random sampling in the phase-encodes’; see the article by Michael Lustig et al. [29].

- *Multi-dimensional NMR spectroscopy.* NMR spectroscopy experiments are more abstract and flexible than MR imaging, and can in principle be designed to encompass arbitrary-dimensional experiments; however, high-dimensional experiments take longer than low-dimensional ones, and practical limitations can intervene: these include denaturing of the sample material, and lack of exclusive access to a spectrometer for the days or weeks that might be required. In practice, experiments at higher dimensions than 3 are rarely attempted.

The FID in a spectroscopy experiment also can be viewed as the sequence of samples along a line in a d -dimensional data hypercube of ‘Fourier’ coefficients. However, the notion of Fourier transform differs in spectroscopy because each coefficient is hypercomplex-valued, so each sampled value $\hat{x}(k_0, \dots, k_{d-1})$ is 2^d -dimensional; for an explanation of this point see [38, 35].

In NMR spectroscopy, anisotropic undersampling has been applied for decades by Jeffrey Hoch and collaborators; see [42, 43, 34, 25].

Mathematical scientists who study compressed sensing often mention MR imaging or NMR spectroscopy as applied settings where undersampled Fourier imaging is indeed applied successfully today; they rarely if ever mention that in either applied setting, the sampling is *always* anisotropic; it *never* makes sense to sample isotropically, because one *always* gets exhaustive samples along one of the dimensions (a.k.a direct dimension) inherently as part of the physical experiment; it makes no sense to throw away measurements that were already mandatorily taken. Mathematical scientists often speak as if isotropic undersampling were an option in these applied settings, and reference theories involving isotropic undersampling. However, in either setting, isotropic sampling is not a sensible option, and the referenced theories do not offer accurate predictions of what happens in real experiments.

In contrast, our results describe anisotropic sampling of the type actually used in these applied fields and give accurate predictions of the sparsity/undersampling relation in undersampled imaging/spectroscopy.

1.6 Relation to Previous Work on Block Diagonal Undersampling

This paper considers precise finite- N phase transition properties of a setting seemingly unrelated to block-diagonal undersampling: anisotropic undersampling in d -dimensional (hypercomplex-) Fourier imaging. It identifies block-diagonal measurement systems as an analysis tool that allows us to make accurate predictions of the behavior of anisotropic undersampling.

Actually, block-diagonal undersampling has been discussed previously as an approach to compressed sensing of interest in its own right. For example, block-diagonal undersampling has been used for compressed image acquisition in [28, 19] and was studied as part of a more general category of compressed sensing, namely tensor compressed sensing, in [20, 27].

There are also interesting theoretical papers on block-diagonal measurement matrices, the main emphasis has been on the Restricted Isometry Property (RIP) for such matrices. For example, see work by Eftekhari et al. [17] and by Adcock and Chun [5]. The RIP offers qualitative insights, and allows these earlier authors to propose the interpretation that, under favorable assumptions,⁴ block-diagonal matrices *asymptotically* “perform nearly as well as dense Gaussian random matrices” for compressed sensing.

Our interpretation of the results we obtain in this paper is quite different. Motivated by anisotropic undersampling in practical d -dimensional (hypercomplex-) Fourier imaging, we study the finite- N phase transitions to learn about the precise sparsity level needed for exact recovery. We then show rigorously that for a special analytically tractable set of situations, the finite- N phase transition is conspicuously different from the phase transitions for dense Gaussian undersampling. Moreover, we derive formulas that predict accurately even outside cases where we can do rigorous mathematical analysis. By extensive computations we document the accuracy of our finite- N prediction formulas and thereby show quite generally that there are substantially worse finite- N phase transitions for anisotropic/block-diagonal undersampling than for Gaussian undersampling. We do find that, asymptotically as N grows *very* large, the finite- N phase transitions of anisotropic undersampling schemes converge to the asymptotic phase transition of Gaussian undersampling; however, this convergence occurs much more slowly than under isotropic sampling.⁵

2 Finite- N Phase Transitions for Block Diagonal Measurements

In this section, we discuss the problem of recovering a sparse N -vector \mathbf{x}_0 from n measurements $\mathbf{y} = A\mathbf{x}_0$. Here the $n \times N$ measurement matrix A has a special block structure and we use a particular convex optimization in our attempt to recover \mathbf{x}_0 . In one special case, we derive the exact finite- N phase transition properties and show that block-diagonal measurement matrices underperform dense *i.i.d* Gaussian matrices by a substantial amount. In later sections, the *ansatz* provided by the explicit formulas derived in this special case are generalized to successfully predict experimental results across all other cases, with similar conclusions.

⁴ These papers assume that signals have sparse representation by incoherent dictionaries such as Fourier or cosine basis

⁵As an example, for an $M \times M$ grid where one of the dimensions is measured exhaustively, the rate of convergence is $M^{-1/2}$, while for isotropic random sampling in both dimensions, this rate would be M^{-2} .

2.1 The convex optimization problem

The data vector \mathbf{y} is assumed to arise by applying the measurement matrix A to the unknown object \mathbf{x}_0 . To reconstruct \mathbf{x}_0 , we solve the following convex optimization problem:

$$(P_{1,\mathbf{X}}) \quad \min \|\mathbf{x}\|_{1,\mathbf{X}} \quad \text{subject to} \quad A\mathbf{x} = \mathbf{y}, \quad \mathbf{x} \in \mathbf{X}^N.$$

Here each coefficient $x(i)$ is supposed to belong to a convex subset $\mathbf{X} \subset \mathbf{R}^k$ with nonempty interior, and $\|\cdot\|_{1,\mathbf{X}}$ denotes the (appropriately defined) “ ℓ_1 norm” on $(\mathbf{R}^d)^N$. The coefficient set \mathbf{X} might for example be $[0, 1]$, $[0, \infty)$, or \mathbf{R} , in which case $d = 1$ and $\|\cdot\|_{1,\mathbf{X}}$ denotes the usual ℓ_1 -norm on \mathbf{R}^N . But we could also have \mathbf{X} be the set of complex numbers \mathbf{C} , or the hypercomplex set \mathbf{H}^d [38, 35]. When \mathbf{X} is \mathbf{C} (resp. \mathbf{H}_d), the ambient dimension k is 2 (resp. 2^d), and $\|\cdot\|_{1,\mathbf{X}}$ denotes what is more usually called the mixed $\ell_{2,1}$ norm: $\|x\|_{2,1} = \sum_{i=1}^N \|x(i)\|_{\ell_2(\mathbf{R}^k)}$ (resp. hypercomplex one-norm $\|x\|_{\mathbf{H},1}$ [38]).

Below, we often write (P_1) rather than $(P_{1,\mathbf{X}})$, making the coefficient domain explicit only where necessary.

2.2 Block-Diagonal Measurement Matrices

In this section, the measurement matrices A will always be in block form:

$$A = \left[\begin{array}{c|c|c|c|c} A^{(1)} & 0 & 0 & \dots & 0 \\ \hline 0 & A^{(2)} & 0 & \dots & 0 \\ \hline & & \dots & & \\ \hline 0 & \dots & 0 & A^{(B-1)} & 0 \\ \hline 0 & \dots & 0 & 0 & A^{(B)} \end{array} \right],$$

where each block $A^{(b)}$ is $m \times M$. The 0’s here also denote $m \times M$ blocks, filled with zero entries. The whole matrix is of size $n = mB$ by $N = MB$, and only the blocks on the diagonal can be nonzero.

We can construct such block diagonal matrices in two ways:

- *Repeated-Block Ensembles (RB)*: Our blocks are simply B identical copies of the same $m \times M$ block.
- *Distinct-Block Ensembles (DB)*: There are B distinct blocks of size $m \times M$.

To obtain the individual blocks, we often consider drawing them at random. A standard construction involves Gaussian *i.i.d* entries $A_{i,j} \sim N(0, \frac{1}{m})$. We often start with such a matrix but then normalize its columns to unit length; formalizing this:

Definition 2.3. A matrix A is said to (have columns sampled from, be sampled from) the Uniform Spherical Ensemble (USE) if its columns \mathbf{a}_i are sampled *i.i.d* from the uniform distribution on the unit sphere $S^{m-1} \subset \mathbf{X}^m$, where \mathbf{X} is either \mathbf{R} or \mathbf{C} .

Using random blocks from USE, the Distinct/Repeated blocks distinction gives us two kinds of matrix ensembles:

- *Repeated-Block USE (RBUSE)*. We draw a *single* block $A^{(1)}$ from USE. We generate a block-diagonal matrix $A = \text{diag}(A^{(1)}, \dots, A^{(1)})$ having all B blocks be identical copies of $A^{(1)}$. Equivalently, the full measurement matrix A is a *Kronecker* product: $A = I_B \otimes A^{(1)}$.
- *Distinct-Block USE (DBUSE)*. We draw B independently-sampled $m \times M$ blocks $A^{(b)}$, $b = 1, \dots, B$, from USE. We generate a block-diagonal matrix $A = \text{diag}(A^{(1)}, \dots, A^{(B)})$. This may equivalently be written as a direct sum: $A = \bigoplus_{b=1}^B A^{(b)}$.

2.4 Separability

Since our measurement matrix A has the block-diagonal form $A = \text{diag}(A^{(1)}, A^{(2)}, \dots, A^{(B)})$, it makes sense to partition the vectors \mathbf{y} and \mathbf{x} involved in the relation $\mathbf{y} = A\mathbf{x}$ consistently with block structure of A :

$$\mathbf{x} = [x^{(1)} \mid x^{(2)} \mid \dots \mid x^{(B)}], \quad \mathbf{y} = [y^{(1)} \mid y^{(2)} \mid \dots \mid y^{(B)}],$$

where the subvectors $x^{(b)}$ are $M \times 1$, while the $y^{(b)}$ are $m \times 1$. The equation $\mathbf{y} = A\mathbf{x}$ is then precisely equivalent to the B different relations

$$y^{(b)} = A^{(b)}x^{(b)}, \quad b = 1, \dots, B.$$

Define now the b -th *block subproblem*:

$$(P_1^{(b)}) \quad \min \|x\|_{1,\mathbf{X}} \quad \text{subject to} \quad A^{(b)}x = y^{(b)}, \quad x \in \mathbf{X}^M.$$

The key consequence of block-diagonality of A is that the optimization problem (P_1) becomes separable into its pieces $(P_1^{(b)})$.

Lemma 2.1. (Separability of (P_1)) *We have*

$$\text{val}(P_1) = \sum_{b=1}^B \text{val}(P_1^{(b)}).$$

Let $\mathcal{X}_1^{(b)} \subset \mathbf{X}^M$ denote the set of optimal solutions of $(P_1^{(b)})$ and let $\mathcal{X}_1 \subset \mathbf{X}^N$ denote the set of solutions of (P_1) . Then

$$\mathcal{X}_1 = \bigoplus_{b=1}^B \mathcal{X}_1^{(b)}.$$

In particular, suppose that each subproblem $(P_1^{(b)})$ has a unique solution $x_1^{(b)}$. The combined vector $\mathbf{x}_1 = [x_1^{(1)} \mid x_1^{(2)} \mid \dots \mid x_1^{(B)}]$ is then the unique solution to (P_1) . Suppose that (P_1) has a unique solution \mathbf{x}_1 . Then the b -th block of \mathbf{x}_1 , say $x_1^{(b)}$, is the unique solution of $(P_1^{(b)})$.

Corollary 2.2. (Product Rule for Success Probabilities) *Suppose that the block matrices $A^{(b)}$, $b = 1, \dots, B$ are sampled i.i.d from a common distribution, and the subvectors $x_0^{(b)}$ are sampled i.i.d from a common distribution. Define the events*

$$\Omega^{(b)} \equiv \{(P_1^{(b)}) \text{ has an unique solution } x_1^{(b)}, \text{ and } x_1^{(b)} = x_0^{(b)}\}$$

(i.e. $\Omega^{(b)} = \{\mathbf{x}_1^{(b)} = \{x_0^{(b)}\}\}$). Correspondingly, let

$$\Omega \equiv \{(P_1) \text{ has an unique solution } \mathbf{x}_1, \text{ and } \mathbf{x}_1 = \mathbf{x}_0\}.$$

Then

$$\Omega = \bigcap_{b=1}^B \Omega^{(b)},$$

and

$$\Pr(\Omega) = \Pr(\Omega^{(1)})^B.$$

For clarity we point out that the matrices $A^{(b)}$ are not assumed by the Corollary to have any specific properties themselves, e.g. they do not have to have *i.i.d* elements $A_{ij}^{(b)}$; instead $A^{(i)}$ is simply assumed to be stochastically independent of $A^{(j)}$.

In a sense, this corollary reduces the task of computing the probability of exact recovery to the task of computing $P(\Omega^{(1)})$.

2.5 Exact Finite- N Success Probabilities for $(P_{1,[0,1]})$

In one very special case, it is possible to evaluate $P(\Omega^{(1)})$ exactly at each M and ℓ . We study this case carefully for clues about the general situation. Consider the (single-block) convex optimization problem:

$$(P_{1,[0,1]}^{(1)}) \quad \min \|x\|_1 \quad \text{subject to} \quad A^{(1)}x = A^{(1)}x_0, \quad 0 \leq x(i) \leq 1.$$

This is an instance of what we earlier called $(P_{1,\mathbf{X}})$ with the specific coefficient set $\mathbf{X} = [0, 1]$. In this problem only, when we say that x_0 has *at most ℓ non-constrained elements*, we mean that at most ℓ coefficients $x_0(i)$ do not belong to the boundary $\{0, 1\}$ of $\mathbf{X} = [0, 1]$.

To proceed further, we need two notions:

- *Exchangeability.* The random variables Z_1, \dots, Z_M are *exchangeable* if, for any permutation P on the set $\{1, \dots, M\}$, the joint probability distribution of $(Z_{P(1)}, \dots, Z_{P(M)})$ is the same as that for (Z_1, \dots, Z_M) .
- *General position.* The vectors $\mathbf{a}_1, \dots, \mathbf{a}_M$ are in *general position* in \mathbf{R}^m if no subcollection of at most m vectors is linearly dependent.

We now describe two conditions, either of which allows exact evaluation of success probabilities.

- (C_A) A is any fixed $m \times M$ matrix with its M columns in general position in \mathbf{R}^m . x_0 is a random M -vector in $[0, 1]^M$ surely having ℓ entries different than 0 or 1, and the joint distribution of $(x_0(i) : 1 \leq i \leq M)$ is exchangeable.
- (C_x) x_0 is any fixed vector in $[0, 1]^M$ having ℓ entries different than 0 or 1. A is a random $m \times M$ matrix whose columns $(\mathbf{a}^{(1)}, \mathbf{a}^{(2)}, \dots, \mathbf{a}^{(M)})$ are almost surely in general position and have an exchangeable joint distribution.

Theorem 2.3. [15] (**Exact Success probabilities in the Single-Block Problem, $\mathbf{X} = [0, 1]$.)** Assume either of assumptions (C_A), (C_x) for the joint distribution of (A, x_0) . Let Ω denote the event that $(P_{1,[0,1]}^{(1)})$ has a unique solution, and that solution is precisely x_0 . Then $\Pr(\Omega)$ depends only on ℓ, m, M , and not on any other details of the joint distribution of (A, x_0) . In fact, $\Pr(\Omega) = Q_{sb}(\ell, m, M; [0, 1])$, where

$$\begin{aligned} Q_{sb}(\ell, m, M; [0, 1]) &= 1 - 2^{-(M-\ell-1)} \sum_{j=0}^{M-m-1} \binom{M-\ell-1}{j} \\ &= 1 - P_{M-m, M-\ell}, \text{ say.} \end{aligned} \quad (1)$$

We now remind the reader that in a sequence of B independent Bernoulli trials with common success probability q , the chance of B consecutive successes is q^B . As a result, we can infer general multiblock success probabilities from single-block ones (under appropriate assumptions).

Lemma 2.4. (Exact Success probabilities in the Multiblock Problem.) Consider a random instance of the multiblock problem $(P_{1,\mathbf{X}})$, where the individual components $(A^{(b)}, x_0^{(b)})$ are i.i.d according to a specific distribution ν .

Let $Q_{sb} = Q_{sb}(\ell, m, M; \nu, \mathbf{X})$ denote the success probability for the single-block problem $(P_{1,\mathbf{X}}^{(1)})$: namely, let $\Omega^{(1)}$ denote the event that $(P_{1,\mathbf{X}}^{(1)})$ has a unique solution, and that solution is precisely $x_0^{(1)}$, and set

$$Q_{sb} = \Pr(\Omega^{(1)}).$$

Let $Q_{mb} = Q_{mb}(B \cdot \ell, B \cdot m, B \cdot M; \nu, \mathbf{X})$ denote the success probability for the multiblock problem $(P_{1,\mathbf{X}})$: i.e., with Ω denoting the event that $(P_{1,\mathbf{X}})$ has a unique solution, and that solution is precisely x_0 , we have

$$Q_{mb} = \Pr(\Omega).$$

Then

$$Q_{mb} = (Q_{sb})^B.$$

Turn now to the corresponding multiblock problem

$$(P_{1,[0,1]}) \quad \min \sum_{b=1}^B \|x^{(b)}\|_1 \quad \text{subject to} \quad A^{(b)}x^{(b)} = y^{(b)}, \quad 0 \leq x^{(b)}(i) \leq 1, \quad 1 \leq b \leq B.$$

Corollary 2.5. Consider a random instance of the multiblock problem $(P_{1,[0,1]})$ where the individual components $(A^{(b)}, x_0^{(b)})$ are i.i.d according to a specific distribution ν that almost surely obeys (C_A) conditionally on A , or almost surely obeys (C_x) conditional on x_0 . Then when $N = B \cdot M$, $n = B \cdot m$, and $k = B \cdot \ell$,

$$Q_{mb}(k, n, N; \nu, [0, 1]) = Q_{sb}(\ell, m, M; [0, 1])^B. \quad (2)$$

Note that the RHS of (2) does not depend on any further details of the joint distribution ν . It is in this sense *universal*.

2.6 Finite- N Phase transition Location for $(P_{1,[0,1]})$

Here is how we obtain estimates of the Finite- N phase transition.

Definition 2.7. Assume that we have experimental data for the frequency of successful reconstruction at a fixed undersampling ratio δ and varying sparsity ratio ϵ , Assume that we fit a generalized linear model

$$\Pr\{\text{Success}|\delta, \epsilon\} = \pi(a + b\epsilon|\delta),$$

to the empirical success frequencies $\hat{Q}(k, n, N)$, where $\pi(\cdot|\delta)$ denotes the fitted distribution.

- In the single-block case, we use the Normal distribution (Probit link).
- In the multi-block case, we use the Gumbel distribution (CLL link).

In the multiblock case we define the special constant $q^* = 1 - 1/e$ and in the single block case, we set $q^* = 1/2$.

Definition 2.8. Consider a random instance of an optimization problem (P) with problem sizes (k, n, N) , where n and N are the extent of the matrix A and k is the number of nonzeros in x_0 . Let $Q(k, n, N)$ denote the probability of success with given size parameters. Let q^* be the probability defined in Definition 2.7. Let k^* denote the smallest integer closest to achieving success probability q^* :

$$Q(k^*, n, N) \approx q^*.$$

The Finite- N phase transition location is the ratio

$$\epsilon^*(n, N; (P)) = \frac{k^*}{N}.$$

We now apply this concept using the formulas of the last section, in two ways. Once, on a ‘classical’ single-block problem, and once on a multiblock problem of equivalent size.

- **Single-Block Problem.** Consider a single-block problem of size $N = BM$, $n = Bm$, $k = B\ell$, which is equivalent to the problem size of a multiblock problem to be considered next. We emphasize that this is not the main case for analysis in this section, but we study it for comparison purposes. It corresponds to the case $N = M$, $B = 1$ in our notation, which is not our usual case. Using the preceding Theorem, the critical number of nonzeros $k_{sb}^*(n, N)$ solves

$$Q_{sb}(k_{sb}^*, n, N) \approx q^*,$$

and we define the single-block Finite- N phase transition by

$$\epsilon_{sb}^* = \frac{k_{sb}^*(n, N)}{N}.$$

- **Multi-Block Problem.** Again in the multiblock setting $B \gg 1$, the preceding corollary shows that the probability of success is a function of ℓ, m, M, B . The critical number of nonzeros $\ell_{mb}^* = \ell_{mb}^*(m, M, B)$, yielding

$$Q_{sb}(\ell_{mb}^*, m, M)^B \approx q^*.$$

Setting $k_{mb}^* = B \cdot \ell^*$ for the equivalent total number of nonzeros and the total problem sizes $n = Bm$, $N = BM$, the phase transition location is

$$\epsilon_{mb}^*(m, M, B) = \frac{k_{mb}^*}{N} = \frac{B \cdot \ell^*}{B \cdot M} = \frac{\ell_{mb}^*(m, M, B)}{M}.$$

To be more concrete, we need specific assumptions about m, M , and B .

Lemma 2.6. Consider a sequence of problem sizes where $B = M$, $M \rightarrow \infty$, and $m/M \rightarrow \delta \in (1/2, 1)$. With $N = B \cdot M$ and $n = B \cdot m$ we have $n \sim \delta N$. Define the asymptotic phase transition

$$\epsilon_{asy}^*(\delta; [0, 1]) = (2\delta - 1)_+.$$

For the single-block finite- N phase transition we have:

$$\epsilon_{sb}^*(m, M; [0, 1]) = \epsilon_{asy}^*(\delta) + O\left(\frac{1}{M}\right).$$

Define $\gamma_M = \sqrt{\frac{2 \log(M)}{M}}$. For the multi-block finite- N phase transition we have

$$\epsilon_{mb}^*(m, M, B; [0, 1]) = \epsilon_{asy}^*(\delta) - \sqrt{2(1 - \delta)} \cdot \gamma_M + o(\gamma_M).$$

Proof. See Appendix A. □

In particular, this lemma shows that as $B = M \rightarrow \infty$ with $m \sim \delta M$,

$$\epsilon_{sb}^*(m, M) - \epsilon_{mb}^*(m, M, B) = \sqrt{2(1 - \delta)} \cdot \gamma_M \cdot (1 + o(1)).$$

Because $\gamma_M \rightarrow 0$ as $M \rightarrow \infty$, this shift in phase transitions locations is asymptotically negligible. However, our experimental observations—given above and also below—show it to be quite substantial in the intended applications. The mismatch between the single-block prediction and the observed behavior in the multiblock case is quite substantial unless M (not N) is large. In applications it is much harder to make M large than to make N large. Note that in the above lemma the system size is $N = BM = M^2$. Hence we may equivalently write

$$\epsilon_{sb}^* - \epsilon_{mb}^* \sim \frac{\sqrt{2(1 - \delta) \log(N)}}{N^{1/4}}, \quad N \rightarrow \infty.$$

The denominator shows that the gap between the two phase transitions closes very slowly with increasing problem size N .

2.9 Nonidentical Subproblems?

Corollary 2.5 showed us that in case the different subproblems $(A^{(b)}, x^{(b)})$ are i.i.d. from a common distribution, simple formulas for the multiblock success probability become available. In applications, as we will discuss later, the different subproblems might not be identical in structure. However, the above formulas provide ample clues for those cases as well, as we will discuss further below.

For example, we can see that, if among the B subproblems, if there were one ‘outlier subproblem’ with dramatically higher fraction of nonzeros $\epsilon^{(b)} = k_b/M$, then that subproblem would likely be the one whose success or failure determined the success or failure of the whole reconstruction. That subproblem would be in a sense the ‘weakest link’.

Following down this path, we see that having identical sparsity fractions and iid matrices $A^{(b)}$ is a kind of extremal situation; in other situations the finite- N phase transition is likely to be worse. We call this situation the regular situation, and because we document a sizeable offset below ϵ_{asy}^* in this situation, one easily sees that other cases will show even larger effects than documented here in Lemma 2.6.

As an example, consider a situation where the vector \mathbf{x} has $\epsilon = k/N$ nonzeros at randomly chosen positions. In particular the different partitions of the block would have different numbers of nonzeros, according to the usual multinomial distribution. Below we call this situation the multinomial situation. We have worked out the offset of the finite- N phase transition below ϵ_{asy}^* , and indeed the offset is even larger in the multinomial case than in the case with equal numbers of nonzeros per block. We leave detailed discussion of the multinomial case for future work.

Below we focus on the regular case, keeping in mind its extremal nature as the block-diagonal situation somehow closest to the fully dense situation.

3 Equivalence with Anisotropic Undersampling

We now discuss the precise equivalence between anisotropic undersampling and block-diagonal undersampling, considering for now only the case of 2D Fourier imaging. We wish to recover an unknown object $x_0 = (x_0(t_0, t_1) : 0 \leq t_i < M)$ with complex-valued entries, defined on a 2D grid of size $M \times M$. Our observations are of the form $\hat{x}_{\text{AUS}}(k_0, i) = \hat{x}(k_0, k_{1,i})$ for some specific choices $\{k_{1,i}, i = 1, m\}$, and for each k_0 satisfying $0 \leq k_0 < M$. Let $\mathbf{C}^{M \times M}$ denote the collection of arrays $x(t_0, t_1)$ with $0 \leq t_0, t_1 < M$, while \mathbf{C}^{M^2} denotes the collection of arrays $\mathbf{x} = (x(i))_{i=1}^{M^2}$.

We think of these measurements $\hat{x}_{\text{AUS}} \in \mathbf{C}^{M \times m}$ as arising from a linear operator \mathcal{F}_{AUS} applied to x_0 : $\hat{x}_{\text{AUS}} = \mathcal{F}_{\text{AUS}}(x_0)$. The operator \mathcal{F}_{AUS} is representable as a pipeline $\mathcal{F}_{\text{AUS}} = \mathcal{S}_2 \circ \mathcal{F}_2$ of two linear operators. The first, \mathcal{F}_2 , say, is simply the usual complex-valued 2D discrete Fourier transform that maps arrays in $\mathbf{C}^{M \times M}$ to their 2D DFT's, also in $\mathbf{C}^{M \times M}$. The second, $\mathcal{S}_{2,M,\mathcal{K}}$, is a selection operator that takes as input an $M \times M$ array, and extracts from it the m rows with indices in $\mathcal{K} = (k_i : 0 \leq i < m)$; here $0 \leq k_i < M$ and the k_i are all distinct). Within each selected row, it exhaustively samples all M elements. The composition $\mathcal{F}_{\text{AUS}} = \mathcal{S}_{2,M,\mathcal{K}} \circ \mathcal{F}_2$ performs anisotropic sampling in 2D-Fourier imaging.

For comparison, let $A^{(1)}$ denote an $m \times M$ block matrix representing the pipeline of two linear operators. The first, \mathcal{F}_1 , performs the usual *one-dimensional* discrete Fourier transform of a vector $v \in \mathbf{C}^M$ delivering a transformed vector $\hat{v} \in \mathbf{C}^M$. The second, $\mathcal{S}_{1,\mathcal{K}}$, takes as input an M -vector (\hat{v} , say) and selects the m entries ($\hat{v}_{k_i} : 1 \leq i \leq m$) out of the M entries available, where $\mathcal{K} = (k_i)_{i=0}^{m-1}$. Further, let A denote the block-diagonal matrix made by repeating the block matrix $A^{(1)}$ along the diagonal M times. Then $A \in \mathbf{C}^{mM \times M^2}$.

Let $\text{vec}() : \mathbf{C}^{M \times M} \mapsto \mathbf{C}^{M^2}$ denote the operator of stacking all the rows of a matrix one by one in one tall vector. Let $\mathbf{x}_0 = \text{vec}(x_0)$, and let $\mathbf{y} = A \cdot \mathbf{x}_0$, so that $\mathbf{y} \in \mathbf{C}^{m \cdot M}$. As $m \cdot M < M^2$, \mathbf{y} is an undersampling of $\mathbf{x}_0 \in \mathbf{C}^{M \times M}$.

The problems of recovering \mathbf{x}_0 from $\mathbf{y} = A \cdot \mathbf{x}_0$ and from $\mathbf{y} = \mathcal{F}_{\text{AUS}}(x_0)$ are not obviously related. One involves a 2D Fourier transformation that is then subsampled, the other involves a stack of separate 1D Fourier transforms.

To connect the two, we need for the element indices selected by $\mathcal{S}_{1,\mathcal{K}}$ in the construction of A to be *identical* to the row indices selected by the anisotropic selection operator $\mathcal{S}_{2,M,\mathcal{K}}$ in the construction of \mathcal{F}_{AUS} .

Theorem 3.1. (Anisotropic undersampling models 2D Fourier Imaging.) *In the construction of A and \mathcal{F}_{AUS} , suppose the underlying indices $(k_i)_{i=1}^m$ used by $\mathcal{S}_{1,\mathcal{K}}$ in the specification of $A^{(1)}$ are the same as the indices $(k_{1,i})_{i=1}^m$ used by $\mathcal{S}_{2,M,\mathcal{K}}$ in the specification of $\mathcal{F}_{\text{AUS}}(\cdot; \mathcal{K})$. Let x_0 be an array in $\mathbf{C}^{M \times M}$, and $\mathbf{x}_0 = \text{vec}(x_0)$ the corresponding array in \mathbf{C}^{M^2} . The following two problems have identical values and isomorphic solution sets:*

$$(P_{1,\mathbf{C}}^{\text{AUS}}) \quad \min \|x\|_{1,\mathbf{C}} \quad \text{subject to} \quad \mathcal{F}_{\text{AUS}}(x) = \mathcal{F}_{\text{AUS}}(x_0), \quad x \in \mathbf{C}^{M \times M},$$

$$(P_{1,\mathbf{C}}) \quad \min \|\mathbf{x}\|_{1,\mathbf{C}} \quad \text{subject to} \quad A\mathbf{x} = A\mathbf{x}_0, \quad \mathbf{x} \in \mathbf{C}^{M^2}.$$

Namely, $\text{val}(P_{1,\mathbf{C}}^{\text{AUS}}) = \text{val}(P_{1,\mathbf{C}})$, and every solution of the first problem is converted into a solution of the second problem by $\text{vec}()$.

Proof. We give two proofs. Appendix C gives a direct proof. Appendix B gives a much more general result of this kind, which is adapted later to prove further results. \square

We point out a very special variant that connects to earlier results.

Corollary 3.2. (Anisotropic undersampling in 2D Fourier Imaging, bounded coefficients.) *In the construction of A and \mathcal{F}_{AUS} , let the underlying indices $k_i, i = 1, \dots, m$ in \mathcal{S}_1 be the same as the indices $k_{1,i}$ used by \mathcal{S}_2 . Let x_0 be an array in $[0, 1]^{M \times M}$ and $\mathbf{x}_0 = \text{vec}(x_0)$. The following two problems have identical values and isomorphic solution sets:*

$$(P_{1,[0,1]}^{\text{AUS}}) \quad \min \|x\|_{1,\mathbf{R}} \quad \text{subject to} \quad \mathcal{F}_{\text{AUS}}(x) = \mathcal{F}_{\text{AUS}}(x_0), \quad x \in [0, 1]^{M \times M},$$

$$(P_{1,[0,1]}) \quad \min \|\mathbf{x}\|_{1,\mathbf{R}} \quad \text{subject to} \quad A\mathbf{x} = A\mathbf{x}_0, \quad \mathbf{x} \in [0, 1]^{M^2}.$$

Lemma 3.3. (T. Tao [46]) *Suppose that M is prime. Then the $m \times M$ matrix $A^{(1)} = \mathcal{S}_1 \circ \mathcal{F}_1$ constructed above has its columns in general position in \mathbf{C}^m .*

Corollary 3.4. *Let M be prime. Let $\mathbf{w}_0 \in [0, 1]^N$ be a random vector of length $N = M^2$ with exactly ℓ entries not equal to 0 or 1 in each M -block. Let \mathbf{x}_0 be a random vector created by randomly permuting the entries of \mathbf{w}_0 in each M -block, via uniformly-distributed random permutations that are stochastically independent from block to block.*

With A the fixed block matrix created above, and \mathbf{x}_0 the random vector described in this Corollary, the assumptions (C_A) and general position of Corollary 2.4 apply. Hence the probability that the solution \mathbf{x}_1 of the multiblock problem $(P_{1,[0,1]})$ is identical to \mathbf{x}_0 is precisely given by the formula

$$\Pr(\{\mathbf{x}_0 = \mathbf{x}_1\}) = Q_{sb}(\ell, m, M; [0, 1])^M.$$

In consequence, our earlier results for block-diagonal undersampling give exact results for success probabilities in anisotropic undersampling. Namely, consider $M \times M$ images ℓ nonzeros thrown down at random within each column. Let $\epsilon_{\text{AUS}}(m, M)$ denote the associated finite- N phase transition for exact recovery in anisotropic undersampling of the object x_0 in 2D-Fourier imaging. This is identical to $\epsilon_{mb}(m, M; M)$. We have:

Corollary 3.5. *Let \mathbf{x}_0 be the random object constructed in the previous corollary. Let W denote an i.i.d Gaussian sensing matrix of size $n \times N$ and let $\mathbf{y}_0 = W\mathbf{x}_0$ denote Gaussian undersampled measurements. Define*

$$(P_{1,[0,1]}^W) \quad \min \|\mathbf{x}\|_{1,\mathbf{R}} \quad \text{subject to} \quad W\mathbf{x} = W\mathbf{x}_0, \quad \mathbf{x} \in [0, 1]^N.$$

Let $\epsilon_W(n, N)$ denote the associated finite- N phase transition for exact recovery from Gaussian undersampling. Then, as M increases, the offset between Gaussian and anisotropic undersampling phase transitions has the following behavior:

$$\epsilon_W(mM, M^2) - \epsilon_{\text{AUS}}(m, M) = \sqrt{2(1 - \delta)} \cdot \gamma_M + o(\gamma_M),$$

where, as above, $\gamma_M = \sqrt{\frac{2 \log(M)}{M}}$.

4 Experimental Approach

The preceding section precisely locates the finite- N phase transition from anisotropic undersampling in one specific case. The finite- N phase transition was shown theoretically to be displaced downwards from the asymptotic Gaussian phase transition by a definite amount, which depends on δ and M .

This formula can be generalized to predict behavior of finite- N phase transitions across a wide range of situations, including general d -dimensional anisotropic sampling and encompassing coefficients that are real, complex and hypercomplex. In all these cases, the formula predicts that the phase transition for anisotropic undersampling is substantially displaced from the phase transition for Gaussian undersampling, by an amount that matters in practically-important problem sizes. The scaling of this offset with M and B is the same in these cases, and the dependence on δ involves in a very particular way the underlying coefficient set \mathbf{X} .

To evaluate the accuracy of these predictions, we developed a framework for massive empirical simulation, which ultimately involved millions of computational experiments. Empirical results are more informative for applications than mathematical proofs would be, as they concern behavior in situations of the scale and type that one might actually encounter, instead of the very large problem sizes typically assumed by asymptotic mathematical analysis, which happen beyond the reach of modern computers and modern NMR experimentation. Our computational framework is consistent with the approach developed in [14, 39].

Though our computational setup allows for an arbitrary number of blocks, in this paper we present results only for the case of $B = M$, which as we have seen corresponds to undersampled 2D-Fourier imaging.

4.1 Predictions of Phase Transition Location

Our formulas for the finite- N phase transition location in block-diagonal undersampling will be stated in terms of deviation from the asymptotic phase transition for Gaussian undersampling. We first make clear what this means, and then we state our formulas.

Formulas for Gaussian Phase Transition. We extend the discussion of Gaussian undersampling from Corollary 3.5, to cover situations of greater generality. Let the $n \times N$ random measurement matrix W have i.i.d $N(0, 1)$ entries ⁶. For

⁶Exactly what this means can be spelled out more precisely in the case of quaternionic or hypercomplex entries, although we do not pause to do so here.

an object $x_0 \in \mathbf{X}^N$, we obtain n measurements $\mathbf{y}_0 = W\mathbf{x}_0$. We attempt reconstruction via

$$(P_{1,\mathbf{X}}^W) \quad \min \|\mathbf{x}\|_{1,\mathbf{X}} \quad \text{subject to} \quad W\mathbf{x} = \mathbf{y}_0, \quad \mathbf{x} \in \mathbf{X}^N.$$

To predict success or failure, we take an asymptotic approach. Consider a sequence of problems indexed by $N \rightarrow \infty$ with $n/N \rightarrow \delta \in (0, 1)$, and in each problem instance let x_0 be k_N -sparse, where $k_N/N \rightarrow \epsilon \in (0, 1)$. Let \mathbf{x}_1 denote the solution of $(P_{1,\mathbf{X}}^W)$ with problem instance (W, \mathbf{x}_0) . The existing literature on compressed sensing gives formulas for the critical sparsity level $\epsilon_{\text{asy}}^*(\delta; \mathbf{X})$ such that, as $N \rightarrow \infty$,

$$\Pr\{\mathbf{x}_1 = \mathbf{x}_0\} \rightarrow \begin{cases} 1 & \epsilon < \epsilon_{\text{asy}}^*(\delta; \mathbf{X}) \\ 0 & \epsilon > \epsilon_{\text{asy}}^*(\delta; \mathbf{X}) \end{cases}.$$

For different choices of \mathbf{X} one can find such formulas in [11, 10, 9, 7, 2]. For example we have already used above the formula $\epsilon_{\text{asy}}^*(\delta; [0, 1]) = (2\delta - 1)_+$.

Formula for regular sparsity. Now return to the block-diagonal undersampling case, where $N = MB$ and the measurement matrix A is block-diagonal, made from B different $m \times M$ blocks. We can partition the underlying vector $x_0 \in \mathbf{X}^N$ into B blocks of size M consistent with those of A . We say that x_0 has *regular sparsity* if it has the same number, ℓ say, of nonzeros in each block. We further assume that x_0 is random, with a block-exchangeable distribution. In this setting our formula states that observed solution to $(P_{1,\mathbf{X}})$ will exhibit, as a function of (\mathbf{X}, m, M, B) ⁷, a finite- N phase transition $\epsilon_{\text{bd}}^*(m, M, B; \mathbf{X})$. Under the assumption that $M \rightarrow \infty$ and $m/M \rightarrow \delta \in (0, 1)$, the predicted offset of the anisotropic undersampling phase transition $\epsilon_{\text{bd}}^*(m, M, B; \mathbf{X})$ ‘below’ the asymptotic transition $\epsilon_{\text{asy}}^*(m/M)$ obeys

$$\frac{\epsilon_{\text{asy}}^*(\delta) - \epsilon_{\text{bd}}^*(m, M, B)}{\epsilon_{\text{asy}}^*(\delta)} = \alpha \cdot \eta(\delta) \cdot \gamma + O(\gamma^2), \quad (3)$$

where $\delta = n/N$, $\gamma = \gamma_{M,B} = \sqrt{2 \log(B)/M}$, $\alpha = \alpha_{\mathbf{X}}$ is a constant given in Table 1 below, and

$$\eta(\delta; \mathbf{X}) = \begin{cases} \epsilon_{\text{asy}}^*(\delta)^{-1} (1 - \epsilon_{\text{asy}}^*(\delta))^{\frac{1}{2}}, & \mathbf{X} = [0, 1] & \delta \in (\frac{1}{2}, 1] \\ \delta^{-\frac{1}{2}} (1 - \epsilon_{\text{asy}}^*(\delta))^{\frac{1}{2}}, & \mathbf{X} = \mathbf{R}_+ & \delta \in (0, 1] \\ \delta^{-\frac{1}{2}}, & \mathbf{X} \in \{\mathbf{R}, \mathbf{C}\} & \delta \in (0, 1] \end{cases}.$$

In the above formulas, $\epsilon_{\text{asy}}^*(\delta) = \epsilon_{\text{asy}}^*(\delta; \mathbf{X})$ denotes the vertical location of the asymptotic Gaussian phase transition for the indicated coefficient set \mathbf{X} . The specific forms of the offset shapes η used here have some precedent⁸ in [16].

Modeling the second order effect. When problem sizes are very small (e.g., $M = B = 100$), we go beyond equation (3) by including a second-order term:

$$\frac{\epsilon_{\text{asy}}^*(\delta) - \epsilon_{\text{bd}}^*(m, M, B)}{\epsilon_{\text{asy}}^*(\delta)} = \alpha \cdot \eta(\delta) \cdot \gamma + \beta \cdot \zeta(\delta) \cdot \gamma^2 + o(\gamma^2), \quad (4)$$

where $\beta = \beta_{\mathbf{X}}$ is a constant given in Table 1, and

$$\zeta(\delta; \mathbf{X}) = \begin{cases} 1, & \mathbf{X} = [0, 1] & \delta \in (\frac{1}{2}, 1] \\ \eta(\delta; \mathbf{X}), & \mathbf{X} \in \{\mathbf{R}_+, \mathbf{R}, \mathbf{C}\} & \delta \in (0, 1] \end{cases}.$$

The additional term, quadratic in γ , leads to improved accuracy in phase transition locations, as will be evident from the plots of Section 5.2.

⁷When $B = M$, we use $\epsilon_{\text{bd}}^*(m, M; \mathbf{X})$ for the purpose of brevity.

⁸ More specifically, Donoho and Tanner in [16] proved finite- N bounds on the probability of failure, and their bounds involve a vertical offset in the (δ, ϵ) plane of finite- N iso-probability contours away from the corresponding large- N phase-transition location. In the case $\mathbf{X} = \mathbf{R}$, their offset is proportional to our offset function $\eta(\delta; \mathbf{R}) = \delta^{-1/2}$. See Appendix E for more details.

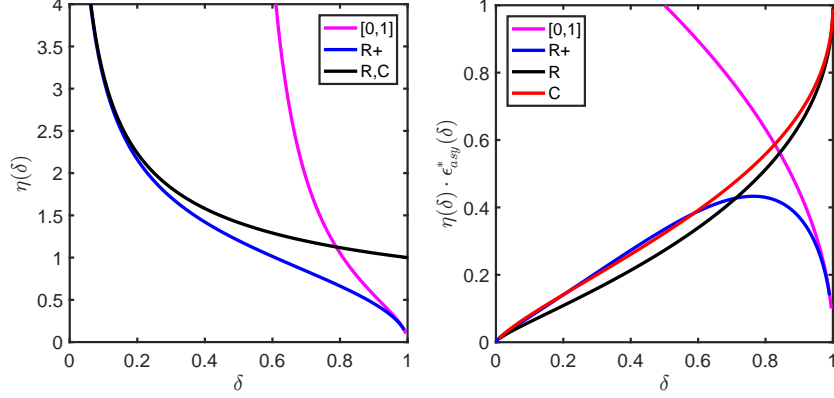


Figure 4: Slope functions in the finite- N prediction formula (3): (left) $\eta(\delta)$, (right) $\eta(\delta) \cdot \epsilon_{\text{asy}}^*(\delta)$

Table 1: Values for $\alpha_{\mathbf{X}}$ and $\beta_{\mathbf{X}}$ used in (4)

\mathbf{X}	$[0, 1]$	\mathbf{R}_+	\mathbf{R}	\mathbf{C}
$\alpha_{\mathbf{X}}$	1	1	1	$2/3$
$\beta_{\mathbf{X}}$	$1/2$	$-1/3$	$-1/2$	$-1/3$

4.2 Experimental Procedure

For each quadruple (k, m, M, B) , and each relevant coefficient ground set \mathbf{X} we run S Monte Carlo trials. In each experiment, we generate a pseudo-random k -sparse object $\mathbf{x}_0 \in \mathbf{X}^N$ according to the regularity constraint r_C . We take undersampled linear measurements, $\mathbf{y}_0 = A\mathbf{x}_0$ where the B blocks of matrix A are each of size $m \times M$ and generated according to a certain random or deterministic sequence. (y, A) provides an instance of $(P_{1, \mathbf{X}})$ that we supply to a convex optimization solver to obtain solution \mathbf{x}_1 . We then compare \mathbf{x}_0 with \mathbf{x}_1 . If the relative error $\|\mathbf{x}_0 - \mathbf{x}_1\|_2 / \|\mathbf{x}_0\|_2 < 0.001$, we declare the reconstruction a success; otherwise we declare it a failure. We thus obtain S binary measurements Y_i indicating success or failure of reconstruction. The empirical success probability is then calculated as

$$\hat{\pi}(k|A, \mathbf{X}) = \frac{\#\text{successes}}{\#\text{trials}} = S^{-1} \sum_{i=1}^S Y_i.$$

Our raw dataset contains these empirical success fractions, at each combination of (k, m, M, B, S) we explored.

4.3 Modeling the Quantal Response Function

In biological assessment, the quantal response measures the probability of organism failure (e.g., death) as a function of drug dose. In the context of compressed sensing, the quantal response gives the probability of failure in reconstruction as a function of the ‘complexity dose’, i.e. the number of nonzeros in the vector \mathbf{x}_0 . This of course is measured by sparsity ratio ϵ . It is shown in [14] that a Probit model adequately describes the quantal response for Gaussian measurement matrices.

For block-diagonal matrices with block-regular sparsity, the failure probability is expected to follow the generalized extreme value distribution, as it involves the product of failure probabilities of individual blocks. Extreme value theory shows that for large B , the Complementary Log Log (CLL) distribution is an appropriate model for quantal response. Given certain problem size (M, B) , that theory states that the expected fractional success rate can be approximated by:

$$\pi(\epsilon|\delta) = \Pr\{\text{Success}|\delta, \epsilon\} = 1 - \exp\{-\exp(a(\delta) + b(\delta) \cdot \epsilon)\}, \quad (5)$$

for certain underlying parameters $a = a(\delta)$, and $b = b(\delta)$. We then define the empirical phase transition location, at each fixed δ , as the sparsity level ϵ at which the success probability $\pi = 1 - 1/e$ (i.e., 63.2%).

4.4 Studying Very Large Problem Sizes

In the results section we compare models (3) and (4) to data. clear understanding of models explaining offsets of order γ and γ^2 . This required data from experiments conducted at a range of problem sizes - in particular large problem sizes. Actually, plausible sizes can easily led to computational difficulties. In a 2D anisotropic undersampling problem on a 768×768 Fourier grid, we would be considering block-diagonal undersampling with parameters $M = B = 768$, in which case $N = 768^2 = 589824$. General-purpose convex optimization solvers such as CVX are not really appropriate for solving such large problems.

Nevertheless, we have been able to get precise information about the behavior of $(P_{1,\mathbf{X}})$ on block-diagonal problems of such large sizes. The key comes in applying Lemma 2.4, which allows us to infer success probabilities for problems of size $N = B \cdot M$, once we know them for problems of size M . In the cases we are studying, $B = M$, so $M = \sqrt{N}$ and we can use computationally modest resources (denominated in terms of \sqrt{N}) to study very large- N problems that would ordinarily require massive investments of computational resources.

Let $Q_{mb}(k, n, N; \nu, \mathbf{X})$ denote the probability of success in the multiblock optimization problem $(P_{1,\mathbf{X}})$ at given $k = B \cdot \ell$, $n = Bm$ and $N = BM$, where the component subproblems are *i.i.d* according to a fixed distribution ν . Let $Q_{sb} = Q_{sb}(\ell, m, M; \nu, \mathbf{X})$ denote the probability of success in a component single-block problem. Lemma 2.4 gives us the equivalence:

$$Q_{mb}(k, n, N) \leq q^* \Leftrightarrow Q_{sb}(\ell, m, M) \leq (q^*)^{1/B}.$$

At first blush, a hypothesis on Q_{mb} —such as the finite- N phase transition—would seem to require evidence from trials in which the multiblock problem $(P_{1,\mathbf{X}})$ of total size $N = B \cdot M$ gets solved. But we have just shown that such a hypothesis on Q_{mb} is equivalent to one on Q_{sb} . We get information about Q_{sb} by solving random instances of a single-block problem of size M . Suppose $k = B \cdot \ell$ and $N = BM$. Then the hypothesis that $\epsilon_{mb}^* < k/N$ is equivalent to $Q_{mb}(k, n, N) < q^*$, which is equivalent to $Q_{sb}(\ell, m, M) < (q^*)^{1/B}$. So we can indeed use single-block problem realizations to shed light on ϵ_{mb}^* .

Generate S independent problem realizations $(A^{(s)}, x_0^{(s)})$, each one a single-block problem instance with size parameters ℓ, m, M . Solve each realization in turn and record the binary success indicators $X_s = 1_{\{x_1^{(s)} = x_0^{(s)}\}}$. These are Bernoulli random variables at some common but unknown success probability, π , say. Let $Y_s = 1 - X_s$ denote the indicator of failure. Calculate the mean failure rate $\bar{Y} = S^{-1} \sum_{s=1}^S Y_s$.

We propose the following statistical test of $H_0 : (1 - \pi)^B \leq q^*$ against $H_1 : (1 - \pi)^B > q^*$. Fix $\alpha > 0$ small (e.g. $\alpha = 1/20$), and let $z_{1-\alpha/2}$ denote the usual $1 - \alpha/2$ quantile of the Normal distribution, so that $z_{.975} \approx 1.96$. Define $\mu = \mu_B = \log(1/q^*)/B$. Reject the hypothesis H_0 if the failure fraction is high:

$$\bar{Y} > \mu + z_{1-\alpha/2} \sqrt{\frac{\mu}{S}}.$$

Accept H_0 if the fraction of failures is low:

$$\bar{Y} < \mu - z_{1-\alpha/2} \sqrt{\frac{\mu}{S}}.$$

Make no decision otherwise.

Derivation: Let $q_B = 1 - (q^*)^{1/B}$, and suppose our variables were distributed as $X_s \sim \text{Ber}((q^*)^{1/B})$, i.e., just on the sharp edge of the asymptotic phase transition at problem size B . Then $Y_s \sim \text{Ber}(q_B)$. Let $T = \sum_{s=1}^S Y_s$; then $T \sim_{\text{approx}} \text{Poi}(\lambda)$, where $\lambda = S \cdot \mu$. By normal approximation to the binomial, when λ is large, $T \sim_{\text{approx}} N(\lambda, \lambda)$. Consequently,

$$\Pr\{T \in [\lambda - z_{1-\alpha/2} \sqrt{\lambda}, \lambda + z_{1-\alpha/2} \sqrt{\lambda}]\} \approx 1 - \alpha,$$

where the approximation gets increasingly good as $\lambda \rightarrow \infty$. The rule we proposed above then follows.

Another way to write the rule sets $T = S \cdot \bar{Y}$. Then we can decide to reject/accept just in case

$$\bar{Y} \notin \mu \cdot \left(1 \pm \frac{z_{1-\alpha/2}}{\sqrt{S \cdot \mu}}\right).$$

The probability of mistaken rejection is approximately α .

5 Results

5.1 Data collection

To efficiently generate the quantal response data for various ensembles, we have developed and used software package Clusterjob (CJ) [36] - a collection of Perl scripts for automating reproducibility and hassle-free submission of massive computational jobs to clusters. Our computational jobs have mainly run on three different clusters at Stanford, namely `sherlock`, `solomon`, and `proclus`. The optimization solvers used include ASP[21, 22], CVX [23], and MOSEK[1]. It is worth mentioning that software package CVX uses SDPT3 and SEDUMI as its main optimization solvers. Our dataset currently includes 29 million rows, which are the results of nearly 35 million Monte Carlo runs for various problem sizes, and ensembles including RBUSE, DBUSE, RBPFT, etc. For experiments involving smaller problem sizes, one row of data contains information such as the probability of successful reconstruction and error in reconstruction for a particular quadruple (ℓ, m, M, B) in the phase space. For data of larger problem sizes, one row contains information such as error in reconstruction and a binary number indicating success or failure for a particular triple (ℓ, m, M) .

5.2 Verifying predictions

Figures 5 through 15 show the comparison of experimental phase transition data against the first-order and second-order predictions for the four different coefficient sets $\mathbf{X} \in \{[0, 1], \mathbf{R}_+, \mathbf{R}, \mathbf{C}\}$. As an example, Figure 5 shows the empirical offset from the asymptotic phase transition location and the corresponding predictions for the case $\mathbf{X} = [0, 1]$, for which precise and mathematically rigorous results were derived in Section 4. In all these cases, the match between the predictions and data is quite good. The figures also show that our second-order correction terms improve the predictions of the phase transition location - especially for smaller problem sizes.

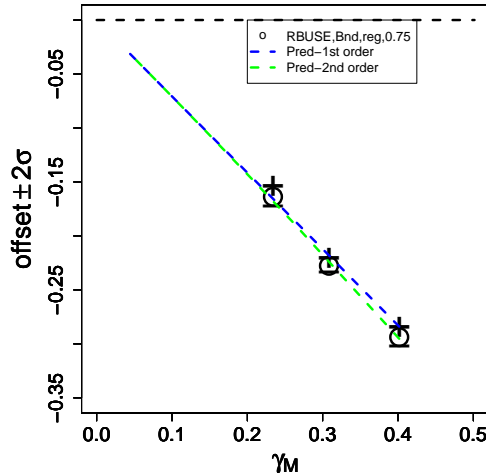


Figure 5: Offset $\epsilon_{\text{asy}}^* - \epsilon_{\text{bd}}^*(m, M)$ versus γ_M for RBUSE ensemble and $\mathbf{X} = [0, 1]$ at $\delta = m/M = 3/4$. Problem sizes: $M = 48, 96$ and 192 . The green and blue curves show the predictions with and without considering the second-order effects, respectively. The plus symbol $+$ locates the $+2s.e.$ confidence bar and minus symbol $-$ locates the $-2s.e.$ limit.

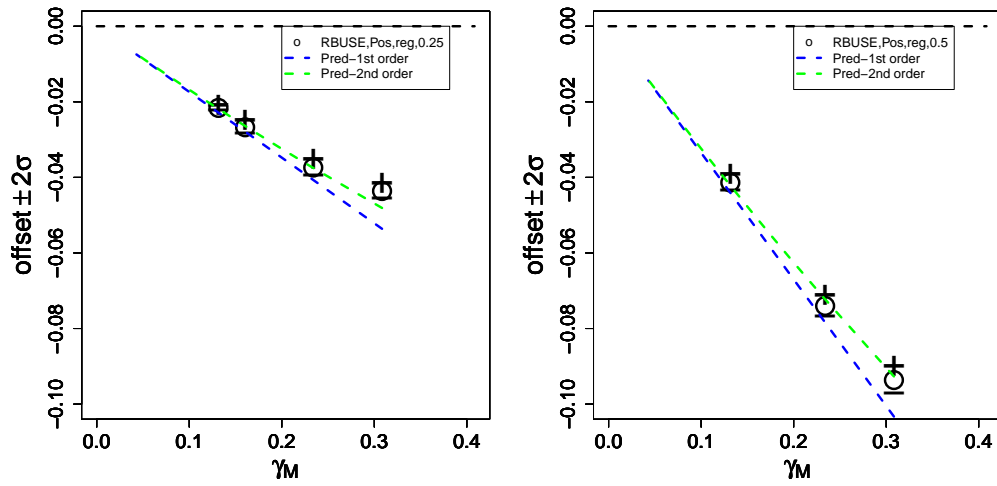


Figure 6: Offset $\epsilon_{\text{asy}}^* - \epsilon_{\text{bd}}^*(m, M)$ versus γ_M for RBUSE ensemble and $\mathbf{X} = \mathbf{R}_+$ at $\delta = 1/2$ (left panel) and $\delta = 1/4$ (right panel). Problem sizes: $M = 96, 192, 480$ and 768 . The green and blue curves show the predictions with and without using the second-order term, respectively. The plus symbol $+$ locates the $+2s.e.$ confidence bar and minus symbol $-$ locates the $-2s.e.$ limit.

+ Positive Coefficients

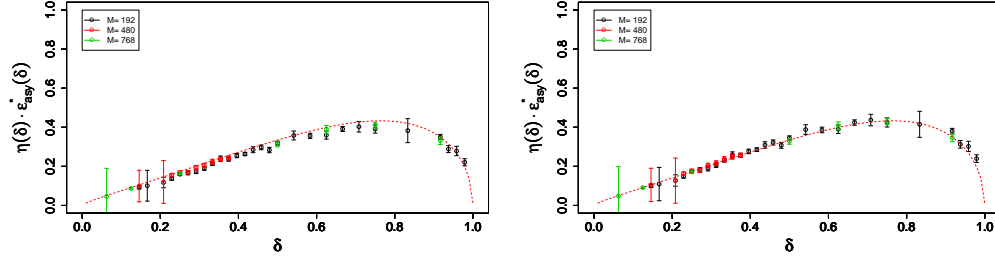


Figure 7: The ratio of offset $\epsilon_{\text{asy}}^* - \epsilon_{\text{bd}}^*(m, M)$ to the first-order coefficient $\alpha\gamma_M$ (left panel) and to the second-order coefficient $(\alpha\gamma_M + \beta\gamma_M^2)$ (right panel) versus undersampling fraction δ . Here, RBUSE ensemble and $\mathbf{X} = \mathbf{R}_+$ coefficient set. Problem sizes: $M = 192, 480$ and 768 . The red dashed curve shows the predicted curves $\eta(\delta) \cdot \epsilon_{\text{asy}}^*(\delta)$.

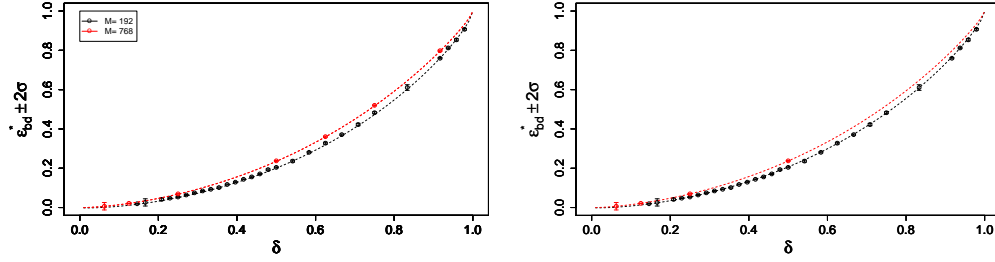


Figure 8: Experimental data against first-order (left), and second-order (right) predictions of phase transition for $\mathbf{X} = \mathbf{R}_+$. Problem sizes: $M = 192, 768$. The circles show data and the dashed lines show predictions.

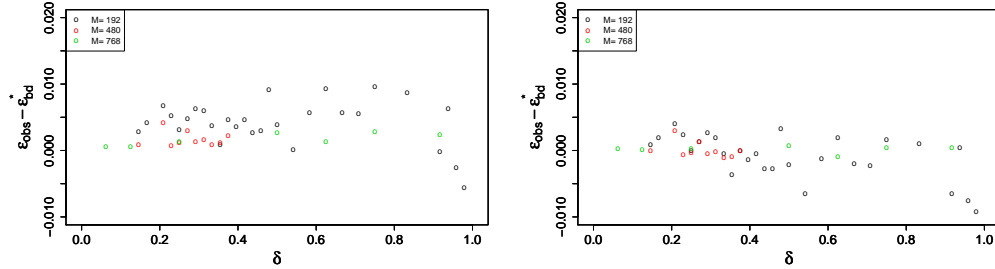


Figure 9: Difference of predicted and experimental phase transition location for $\mathbf{X} = \mathbf{R}_+$ using first-order (left), and second-order (right) predictive models. Problem sizes: $M = 192, 480$ and 768 . Residuals are larger near $\delta \approx 1$, the residuals at $M = 768$ and large δ are noticeably smaller than those at $M = 192$.

+ Real Coefficients

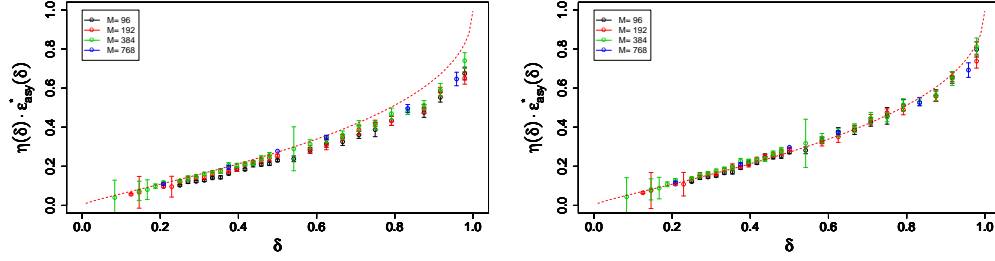


Figure 10: The ratio of offset $\epsilon_{\text{asy}}^* - \epsilon_{\text{bd}}^*(m, M)$ to $\alpha\gamma_M$ (left panel-first order) and $(\alpha\gamma_M + \beta\gamma_M^2)$ (right panel-second order) versus undersampling δ for RBUSE ensemble and $\mathbf{X} = \mathbf{R}$. Problem sizes $M = 96, 192, 384$ and 768 . The red dashed curve shows the predicted curves $\eta(\delta) \cdot \epsilon_{\text{asy}}^*(\delta)$.

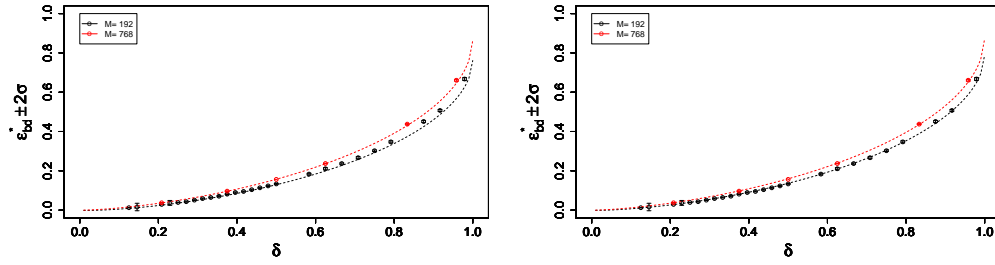


Figure 11: Experimental data against first-order (left), and second-order (right) predictions of phase transition for $\mathbf{X} = \mathbf{R}$. Problem sizes: $M = 192, 768$. The circles are data and the dashed lines are predictions.

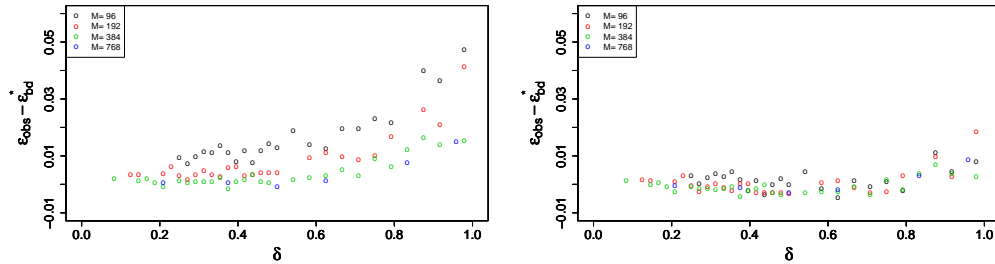


Figure 12: Difference of predicted and experimental phase transition location for $\mathbf{X} = \mathbf{R}$ using first-order (left), and second-order (right) predictive models. Problem sizes $M = 96, 192, 384$ and 768 . Residuals are larger near $\delta \approx 1$, the residuals at $M = 768$ and large δ are noticeably smaller than those at $M = 96$.

+ Complex Coefficients

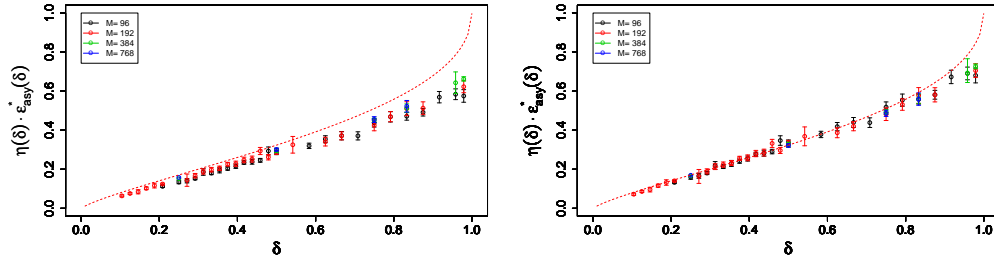


Figure 13: The ratio of offset $\epsilon_{\text{asy}}^* - \epsilon_{\text{bd}}^*(m, M)$ to $\alpha\gamma_M$ (left panel-first order) and $(\alpha\gamma_M + \beta\gamma_M^2)$ (right panel-second order) versus undersampling δ for RBUSE ensemble and $\mathbf{X} = \mathbf{C}$. Problem sizes $M = 96, 192, 384$ and 768 . The red dashed curve shows the predictive curves $\eta(\delta) \cdot \epsilon(\delta)$.

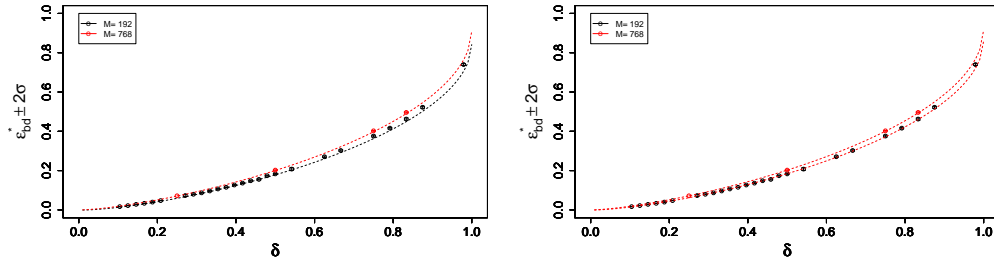


Figure 14: Experimental data against first-order (left), and second-order (right) predictions of phase transition for $\mathbf{X} = \mathbf{C}$. Problem sizes: $M = 192, 768$. The circles are data and the dashed lines are predictions.

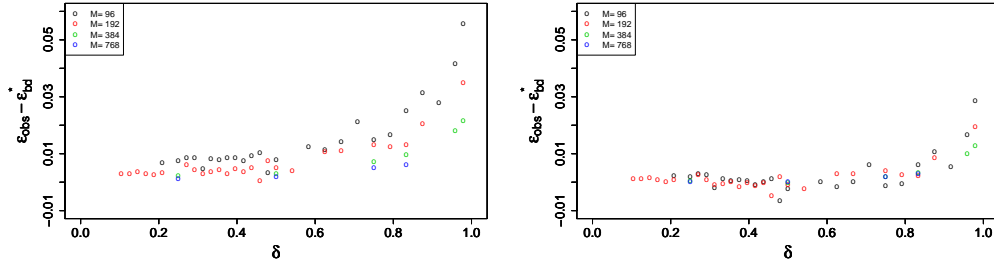


Figure 15: Difference of experimental and predicted phase transition location for $\mathbf{X} = \mathbf{C}$ using first-order (left), and second-order (right) predictive models. Problem sizes $M = 96, 192, 384$ and 768 . Residuals are larger near $\delta \approx 1$, the residuals at $M = 768$ and large δ are noticeably smaller than those at $M = 96$.

6 Stylized Application to MR Imaging

Numerous researchers [48, 50, 49, 45, 18] have been conducting MR imaging experiments where one dimension is sampled exhaustively and the others are sampled at random, and in some cases uniformly at random exactly as discussed here; see for example [29].

Theorem 3.1 shows that the $2D$ Fourier imaging with anisotropic undersampling is equivalent to block-diagonal measurements with $B = M$ and $N = M^2$. This equivalence is illustrated in Figure 2. As expected, the empirical phase transition of the anisotropically-undersampled $2D$ FT is substantially below the transition point for Gaussian measurement matrices.

The $2D$ imaging situation corresponds to the case where $\mathbf{X} = \mathbf{C}$ and $\gamma_M = \sqrt{2 \log(M)/M}$. In the case of $\|\cdot\|_{1,\mathbf{C}}$ minimization our formulas give the following offset between the asymptotic phase transition and the finite- N transition:

$$\begin{aligned} \text{offset} &\sim \alpha_{\mathbf{C}} \cdot \eta(\delta; \mathbf{C}) \cdot \gamma_M + \beta_{\mathbf{C}} \cdot \zeta(\delta; \mathbf{C}) \cdot \gamma_M^2 \\ &= \delta^{-1/2} \left[\frac{2}{3} \gamma_M - \frac{1}{3} \gamma_M^2 \right] \\ &= \delta^{-1/2} \left[\frac{2\sqrt{2}}{3} \sqrt{\frac{\log(M)}{M}} - \frac{2 \log(M)}{3M} \right]. \end{aligned}$$

The experiments reported here validated the formalism's predictions, which can thus be used to gauge the amount of undersampling required in $2D$ imaging experiments.

Lustig and Pauly [29] also proposed anisotropic undersampling for $3D$ MR imaging, where one dimension is acquired exhaustively and the other two are acquired uniformly at random [29]. Our formalism applies to $3D$ MR imaging, where $\mathbf{X} = \mathbf{C}$, $B = M$, $N = M^3$, and $\gamma_M = \sqrt{2 \log(M)/M^2}$.

$$\begin{aligned} \text{offset} &\sim \alpha_{\mathbf{C}} \cdot \eta(\delta; \mathbf{C}) \cdot \gamma_M + \beta_{\mathbf{C}} \cdot \zeta(\delta; \mathbf{C}) \cdot \gamma_M^2 \\ &= \delta^{-1/2} \left[\frac{2}{3} \gamma_M - \frac{1}{3} \gamma_M^2 \right] \\ &= \delta^{-1/2} \left[\frac{2\sqrt{2}}{3} \frac{\sqrt{\log(M)}}{M} - \frac{2 \log(M)}{3M^2} \right]. \end{aligned}$$

The leading term involves $1/M = 1/N^{1/3}$ in the $3D$ case, replacing the leading term $1/\sqrt{M} = 1/N^{1/4}$ from the $2D$ case.

Note: a referee has emphasized that the model of sparsity entertained here is appropriate for images that look like hot spots scattered at random. This might be appropriate for imaging with contrast agents. Further work should study other image models and consider finite- N phase transition phenomena they induce; see also Section 9.

7 Stylized Application to MR Spectroscopy

Jeffrey Hoch and collaborators have used anisotropic random undersampling in multi-D NMR spectroscopy for more than two decades [42]. In MR Spectroscopy, anisotropic undersampling is not the full story; we must also consider the Hypercomplex nature of object \mathbf{x} .

A d -dimensional experiment collects measurements on an array x_0 indexed by a d -dimensional grid of size $T_0 \times \dots \times T_{d-1}$, and having hypercomplex entries. Each hypercomplex entry is a 2^d -dimensional vector over the real field \mathbf{R} ⁹.

⁹Traditionally, the complete set of measurements in MR spectroscopy is a set of $2^{d-1} \cdot \left(\prod_{1 \leq i < d} T_i \right)$ FID's; different FID's are indexed by $(\ell; k_1, \dots, k_{d-1})$. Each FID $F_{k_1, \dots, k_{d-1}}^\ell(\cdot)$ is a complex-valued time series ($F_{k_1, \dots, k_{d-1}}^\ell(k_0) : 0 \leq k_0 < T_0$) and measures two real coordinates of the hypercomplex entry associated with site $(k_0, k_1, \dots, k_{d-1})$ as k_0 varies, effectively sampling along an axis-oriented line $u \mapsto (u, k_1, \dots, k_{d-1})$ in $\mathbf{Z}_{T_0} \times \dots \times \mathbf{Z}_{T_{d-1}}$. Traditional full acquisition requires 2^{d-1} full passes along each line, each pass - indexed by $\ell = 0, 1, \dots, 2^{d-1} - 1$ - measuring a different pair of coordinates of the full 2^d -dimensional entry associated with a given site. In effect, the full d -dimensional hypercomplex transform $\mathcal{F}_{d, \mathbf{H}^d}(x_0)$ is obtained at element $(k_0, k_1, \dots, k_{d-1})$ by gluing together the FID's

$$\hat{\mathbf{x}}(k_0, k_1, \dots, k_{d-1}) = \left(\text{re}(F^0), \text{im}(F^0), \text{re}(F^1), \text{im}(F^1), \dots, \text{re}(F^{2^{d-1}-1}), \text{im}(F^{2^{d-1}-1}) \right),$$

where, in this display, $F^\ell \equiv F_{k_1, \dots, k_{d-1}}^\ell(k_0)$.

In NMR spectroscopy, anisotropic undersampling is generally called *NUS* (for *non-uniform sampling*) [42]. To carry it out, simply sample uniformly at random without replacement from the set of $d - 1$ tuples (k_1, \dots, k_{d-1}) and then collect 2^{d-1} FIDs at each such tuple - $\ell = 0, \dots, 2^{d-1} - 1$ - i.e. collecting each $F_{k_1, \dots, k_{d-1}}^\ell(\cdot)$ associated to each selected tuple. Theorem 3.1 can be generalized as follows, although we omit details in this article.

Let $N = \prod_{i=0}^{d-1} T_i$ and suppose that n is divisible by T_0 . From the collection of $d - 1$ tuples (k_1, \dots, k_{d-1}) in $\mathbf{Z}_{T_1} \times \dots \times \mathbf{Z}_{T_{d-1}}$, sample uniformly at random $m = n/T_0$ such tuples; and let \mathcal{K} denote the resulting set of selected tuples. Let $\mathcal{S}_d \equiv \mathcal{S}_{d, T_0, \mathcal{K}}$ denote the selection operator that, from a full array indexed by d -tuples $(k_0, k_1, \dots, k_{d-1})$ selects all the elements with indices in the product set $\{0, \dots, T_0 - 1\} \times \mathcal{K}$. In this setting, let \mathcal{F}_{AUS} denote the linear operator defined by the pipeline $\mathcal{F}_{\text{AUS}} = \mathcal{S}_{d, T_0, \mathcal{K}} \circ \mathcal{F}_{d, \mathbf{H}^d}$.

For comparison, let $\mathcal{S}_{d-1, \mathcal{K}}$ denote a selection operator on $(d - 1)$ -dimensional arrays indexed by $d - 1$ tuples (k_1, \dots, k_{d-1}) in $\mathbf{Z}_{T_1} \times \dots \times \mathbf{Z}_{T_{d-1}}$. It selects just those entries with indices in \mathcal{K} . Let $\mathcal{F}_{d-1, \mathbf{H}^d}$ denote the $d - 1$ -dimensional discrete Fourier transform *with scalars in the associative algebra \mathbf{H}^d* (and *not \mathbf{H}^{d-1}*), and let $A^{(1)}$ denote the $m \times M$ matrix with \mathbf{H}^d -valued entries representing the linear operator $\mathcal{S}_{d-1, \mathcal{K}} \circ \mathcal{F}_{d-1, \mathbf{H}^d}$. Construct the $n \times N$ block-diagonal matrix A with $B = T_0$ identical blocks $A^{(1)}$; each block is a short fat matrix with hypercomplex \mathbf{H}^d entries of size $m \times M$ with $m = n/T_0$ and $M = N/T_0$.

Theorem 7.1. (Multi-D NUS) *Suppose that the same set \mathcal{K} of $d - 1$ tuples is used in defining both of the above-mentioned selection operators $\mathcal{S}_{d-1, \mathcal{K}}$ and $\mathcal{S}_{d, T_0, \mathcal{K}}$. Let x_0 be a hypercomplex array, and $\mathbf{x}_0 = \text{vec}(x_0)$. The following two problems have identical values and isomorphic solution sets:*

$$(P_{1, \mathbf{X}}^{\text{AUS}}) \quad \min \|x\|_{1, \mathbf{X}} \quad \text{subject to} \quad \mathcal{F}_{\text{AUS}}(x) = \mathcal{F}_{\text{AUS}}(x_0),$$

$$(P_{1, \mathbf{X}}) \quad \min \|\mathbf{x}\|_{1, \mathbf{X}} \quad \text{subject to} \quad A\mathbf{x} = A\mathbf{x}_0.$$

where $\mathbf{X} \in \{[0, 1], \mathbf{R}_+, \mathbf{R}, \mathbf{H}^d\}$ define the choice of the ℓ_1 norm.

Proof. See Appendix D. □

As an example, Figure 16 shows such equivalence for $\mathbf{X} = \mathbf{R}$ and the special case of NUS in 2D experiments (with hypercomplex FIDs) when only half of the indirect times are sampled (i.e., $\delta = 1/2$). Here, the equivalent block diagonal matrix in Theorem 7.1 consists of $B = 2T$ repeated blocks of size $m \times M = T \times 2T$. Each repeated block is a real-valued matrix implementing a partial 1D complex discrete Fourier transform (in this representation, each complex entry in the complex DFT matrix is replaced by its equivalent 2×2 real matrix). We label this block diagonal matrix by ‘RBRealDFT’. The figure documents the equivalence of NUS with ‘RBRealDFT’. The figure also documents performance with the RBUSE block-diagonal measurement matrix where, in place of each partial Fourier matrix we insert a random USE matrix. The results are similar; this is an instance of the universality phenomenon discovered in [12, 39]. For more results of this kind, see [35].

8 In $d > 2$, how many dimensions to randomly undersample?

We plan a full report on the multidimensional case elsewhere, documenting the accuracy of the prediction formalism developed here. The key points can already be seen. Suppose the object of interest is a d -dimensional array, with sidelength T on each axis, so the total data volume $N = T^d$. In anisotropic undersampling of such an array, let $B = T^{d_e}$ where d_e is the number of exhaustively sampled dimensions; the individual blocks themselves are then of dimension $M = T^{d_r}$, where $d_r = d - d_e$. Our *ansatz* for the location of the finite- N phase transition in Lemma 2.6 translates to this special case as follows:

Corollary 8.1. (General $d \geq 2$). *Let $d \in \{2, 3, 4, \dots\}$, and fix $0 \leq d_e, d_r \leq d$, such that $d_r + d_e = d$. Consider a sequence of problem sizes $T \rightarrow \infty$ and associated block-diagonal matrices with $B = T^{d_e}$ blocks of equal size $m \times M$, and with $m/M \rightarrow \delta \in (0, 1)$. For the offset between the asymptotic phase transition $\epsilon_{\text{asy}}^*(\delta; [0, 1])$ and the multi-block finite- N phase transition $\epsilon_{\text{mb}}^*(m, M, B; [0, 1])$ we have:*

$$\epsilon_{\text{asy}}^*(\delta) - \epsilon_{\text{mb}}^* \sim \sqrt{\frac{4 \frac{d_e}{d} (1 - \delta) \log(N)}{N^{d_r/d}}}, \quad N \rightarrow \infty.$$

Two comments are in order:

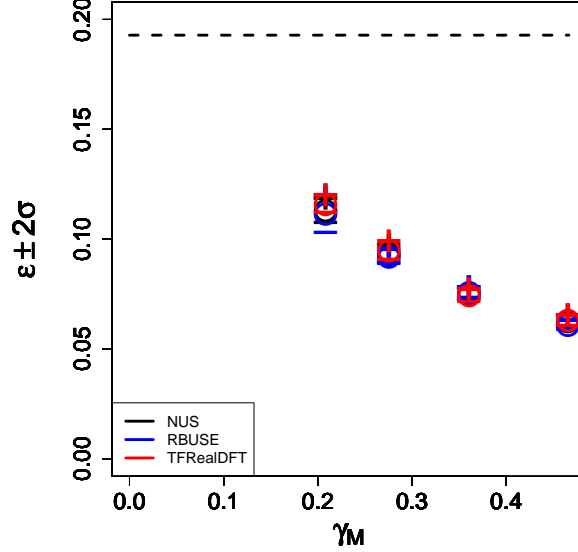


Figure 16: Equivalence of standard undersampling schemes in 2D MR Spectroscopy with anisotropic undersampling schemes involving block-diagonal measurements. The data come from a $T \times T$ Cartesian grid, amounting to $4T^2$ real coefficients. The undersampling fraction $\delta = 1/2$. ‘NUS’ models undersampling of the indirect dimension in MR Spectroscopy, selecting at random half of the $y = \text{constant}$ lines to be measured. ‘RBRealDFT’ corresponds to block-diagonal measurements with $B = 2T$ repeated blocks of size $T \times 2T$, each block the real representation of a partial 1D complex Fourier matrix, in which each complex entry is replaced by its equivalent 2×2 real matrix. ‘RBUSE’ corresponds to block-diagonal measurements with $2T$ identical blocks, each block an $T \times 2T$ real USE matrix. The dashed line represents the asymptotic Gaussian phase transition at $\delta = 1/2$. Problem sizes: $N = 16, 32, 64, 128$.

- Comparing two schemes with equivalent n/N and N , but different d_e , we see that this gap is increasing in the quantity d_e/d . In words: other things being equal, the gap is larger when there are more exhaustively sampled dimensions and hence fewer randomly sampled dimensions.
- Comparing two problems with the same d_e but different d , we see that the gap is relatively less important when d is larger. For example, in multidimensional MR spectroscopy, the gap between the asymptotic Gaussian-measurements phase transition and the finite- N phase transition is larger in smaller dimensions d than in larger dimensions. The order of the gap in 2D-MRI – where $d_e = 1$, $d_r = 1$ – is $O(\sqrt{\log(N)}N^{-1/4})$; while in 3D MRI – where $d_e = 1$, $d_r = 2$ – it is $O(\sqrt{\log(N)}N^{-1/3})$.

9 Limitations of Our Work

There are several ways this study has been more limited than we would like. Here are some possible variations and extensions:

1. *Pixel sparsity.* We have considered here only situations where the object of interest is sparse in the original pixel/voxel domain. This is a very specific assumption, and makes most sense for NMR spectroscopy when the exponential decay times are very long. It also makes sense for MR Imaging with contrast agents where we are looking for relatively rare ‘hotspots’.
2. *Transform Sparsity.* Referees suggested that sparsity in a transform basis would be more general and more widely applicable. We leave this for further work, expecting that results of the precision we have been deriving here would require very specific assumptions.
3. *Uniform Sparsity.* Referees suggested that non-uniform sparsity – i.e. different amounts of sparsity in different blocks – would be more general and more applicable. We agree, and have performed extensive experiments where the sparse signals are scattered randomly, leading to multinomial counts in the different blocks. We

also developed theory for the multinomial case, showing how the first- and second- order correction terms will change. Those terms are somewhat different than before, however, the larger point remains the same: there are precise corrections of order $\text{polylog}(M)/\sqrt{M}$ which we can predict accurately.

We remind the reader that the regular case here is extremal – other nonuniform sparsity cases will have phase transitions that are even lower than this one. On the other hand, our analysis of block-diagonal systems in Section 2 above suggests that if there are dramatic differences in nonzeros from one column to another, what really matters is the maximal number of nonzeros in any column.

All these directions of extension seem worth pursuing.

Finally we remind the reader of the existing theoretical work on block diagonal undersampling - Eftekhari et al. [17] and by Adcock and Chun [5] - which, taking a large- N viewpoint and thereby viewing $\log N$ factors as relatively inconsequential, explicitly claims that anisotropic undersampling is effectively just as good as dense Gaussian undersampling. The deviations from the asymptotic model that we exhibit in Figure 16 above, and which seem practically consequential to us, would be considered *de minimis* from that theoretical viewpoint.

10 Conclusion

We formalized the notion of anisotropic undersampling in multi-dimensional Fourier imaging, and showed its mathematical equivalence with the use of block-diagonal measurement matrices in compressed sensing.

We rigorously analyzed a special case of block-diagonal measurement matrices where the object of interest has real coefficients bounded between 0 and 1 and typically at the extreme values 0 and 1, and derived a precise expression for the finite- N phase transition, finding it to be displaced substantially from the large- N phase transitions applicable fully dense Gaussian measurement schemes.

Massive computational experiments involving millions of CPU hours established the empirical equivalence of random anisotropic Fourier undersampling with block diagonal Gaussian measurements. The experiments showed that the phenomenon of substantial finite- N phase transition offset from the fully dense Gaussian measurement case - proven theoretically in the above special case - continues to hold empirically across a range of other settings, including the recovery of sparse objects with real coefficients, with real nonnegative coefficients or complex coefficients. The experiments allowed us to validate precise formulas for the finite N -phase transitions adapted to all those cases, including second-order [in γ] versions of our formulas matching the experimental data closely.

We presented formulas for the location of finite- N phase transitions in 2D and 3D Sparse MRI, where anisotropic undersampling has a long history and has been extensively used. We briefly discussed multi-dimensional MR spectroscopy, which involves anisotropic undersampling of the hypercomplex Fourier transform, and we empirically demonstrated its equivalence to block-diagonal Gaussian measurements in the 2D hypercomplex case. We left detailed discussion of the multidimensional hypercomplex case for future work.

Reproducible Research

The code and data that generated the figures in this article may be found online at <https://purl.stanford.edu/th702qm4100> [37].

A Proof Sketches for Lemmas 2.6 and 8.1

As the reader will see, the proof is mostly an exercise in manipulating properties of the Binomial distribution and its normal approximation.

A.1 The Single-Block Problem

The critical ℓ -value $\ell^*(m, M)$ for the single block problem solves

$$Q_{sb}(\ell^*, m, M) \approx q^*.$$

Namely, for fixed q^* we find adjacent integers ℓ_{\pm} so that $Q_{sb}(\ell_+, m, M) \geq q^*$ and $Q_{sb}(\ell_-, m, M) \leq q^*$. Then $\ell^* \in \{\ell_-, \ell_+\}$.

Recall that $Q_{sb}(\ell, m, M) = 1 - P_{M-m, M-\ell}$ with $P_{M-m, M-\ell}$ a binomial probability defined in Theorem 2.3. Since we are in the single-block problem, we take $q^* = 1/2$ as explained in Definition 2.7. Hence we are trying to solve for the ℓ_{\pm} achieving

$$P_{M-m, M-\ell_{\pm}} \approx \frac{1}{2}.$$

The binomial probability $P_{k,n}$ is decreasing as n increases for fixed k . Moreover if n is even, then $P_{n/2, n} = 1/2$ exactly. We conclude that when $M - \ell = 2(M - m)$ we will exactly solve $P = 1/2$. We of course do this by setting

$$\ell^* = 2m - M.$$

Then from $\delta \sim m/M$, we get

$$\ell^*/M \sim (2\delta - 1),$$

and so

$$\epsilon_{sb}^*(m, M; [0, 1]) \mapsto (2\delta - 1)_+,$$

as $m, M \rightarrow \infty$ with $m/M \rightarrow \delta$.

A.2 The Multi-Block Problem

The critical value ℓ^* for the multi-block problem and regular sparsity is given by

$$Q_{mb}(B \cdot \ell^*, B \cdot m, B \cdot M) = Q_{sb}(\ell^*, m, M)^B \approx q^*.$$

Namely, either $Q_{mb}(B \cdot \ell^*, B \cdot m, B \cdot M)$ just barely exceeds q^* but $Q_{mb}(B \cdot (\ell^* + 1), B \cdot m, B \cdot M)$ does not, or else $Q_{mb}(B \cdot \ell^*, B \cdot m, B \cdot M)$ barely is below q^* but $Q_{mb}(B \cdot (\ell^* - 1), B \cdot m, B \cdot M)$ is not. Let $\ell_- \equiv \ell_-(B; m, M)$ and $\ell_+ \equiv \ell_+(B; m, M)$ denote the two adjacent integers just identified, namely the smallest ℓ where $Q \leq q^*$ and the largest ℓ where $Q \geq q^*$. Then $\ell^* \in \{\ell_-, \ell_+\}$.

We are interested in the setting where the number of blocks $B \rightarrow \infty$; since q^* is fixed, (e.g. at $1 - 1/e$), it follows that the success probability for individual blocks obeys

$$Q_{sb}(\ell_+, m, M) \geq (q^*)^{1/B} \geq Q_{sb}(\ell_-, m, M). \quad (6)$$

The last display shows that $Q_{sb}(\ell_+(B; m, M), m, M)$ tends to 1 as B increases. However, by standard properties of the Binomial probability mass function and the fact that $\ell_- - \ell_+ = 1$, we also have $Q_{sb}(\ell_-(B; m, M), m, M) \rightarrow 1$. We conclude that the failure probability for individual blocks, $P_{M-m, M-\ell_{\pm}}$, tends to zero.

We first operate purely heuristically to derive the would-be formula, which we then verify rigorously. Taking logarithms of (6), and recalling $Q_{sb}(\ell, m, M) = 1 - P_{M-m, M-\ell}$, then from $-\log(1 - p) \approx p$ for p small, we arrive at an approximation of the following form:

$$P_{M-m, M-\ell_{\pm}} \approx \frac{\log(1/q^*)}{B}.$$

The binomial distribution is approximated by a Gaussian distribution for suitably large problem sizes:

$$\begin{aligned} P_{M-m, M-\ell_{\pm}} &\approx \Phi\left(\frac{(M-m) - \left(\frac{M-\ell_{\pm}}{2}\right)}{\frac{\sqrt{M-\ell_{\pm}}}{2}}\right) \\ &= \Phi\left(\frac{M-2m+\ell_{\pm}}{\sqrt{M-\ell_{\pm}}}\right). \end{aligned} \quad (7)$$

Now, let $z_B = \Phi^{-1}\left(\frac{\log(1/q^*)}{B}\right)$. A continuum approximation ℓ_0 to the finite- N phase transition location, say, is found by solving,

$$\frac{M-2m+\ell_0}{\sqrt{M-\ell_0}} = z_B,$$

which yields,

$$\ell_0 = 2m - M - \frac{1}{2} \sqrt{z_B^4 + 8z_B^2(M-m)} - \frac{z_B^2}{2}. \quad (8)$$

Assuming $|\ell^* - \ell_0| \leq C$, dividing both sides by M and letting $\delta = m/M$:

$$\begin{aligned} \epsilon_{mb}^*(m, M, B, [0, 1]) &= 2\delta - 1 - \frac{1}{2} \sqrt{\left(\frac{z_B^2}{M}\right)^2 + \frac{8z_B^2(M-m)}{M^2}} - \frac{z_B^2}{2M} + O\left(\frac{1}{M}\right) \\ &= 2\delta - 1 - |z_B| \frac{\sqrt{2(1-\delta)}}{\sqrt{M}} + O\left(\frac{z_B^2}{M}\right) \\ &= \epsilon_{sb}^*(m, M; [0, 1]) - |z_B| \frac{\sqrt{2(1-\delta)}}{\sqrt{M}} + O\left(\frac{z_B^2}{M}\right). \end{aligned} \quad (9)$$

For B large, we use the following classical approximation to z_B :

$$|z_B| = \sqrt{2 \log(B)} \cdot (1 + o(1)), \quad B \rightarrow \infty.$$

Setting $\gamma = \sqrt{\frac{2 \log(B)}{M}}$ gives:

$$\epsilon_{mb}^*(m, M, B; [0, 1]) = \epsilon_{sb}^*(m, M; [0, 1]) - \sqrt{2(1-\delta)}\gamma + o(\gamma). \quad (10)$$

To justify the above heuristic derivation rigorously, we need the following four lemmas, which are stated in usual language familiar to probabilists.

Lemma A.1. For $0 < k < n/2$, let $P_{k,n}$ be the usual binomial probability $2^{-n} \sum_{h=0}^k \binom{n}{h}$ and let $\Phi_{k,n} \equiv \Phi((2k-n)/\sqrt{n})$ be its usual normal approximation. We have

$$|P_{k,n} - \Phi_{k,n}| \leq \frac{.26}{n} + e^{-\sqrt{n}}. \quad (11)$$

This Lemma is effectively equation (4) in W. Feller's 1945 paper on Normal approximation to the Binomial; he attributes this to Uspensky.

Lemma A.2. For $0 < k < n/2$, again with $P_{k,n}$ the usual binomial probability,

$$P_{k,n+h} \leq P_{k,n} \cdot 2^{-h} (1 - k/n)^{-h}. \quad (12)$$

Proof. One computes the ratios $r_{k,n+h} = p_{k,n+h}/p_{k,n}$ of probability mass functions. Note that

$$r_{\ell,n+1} = \frac{p_{\ell,n+1}}{p_{\ell,n}} = \frac{2^{-(n+1)} \binom{n+1}{\ell}}{2^{-n} \binom{n}{\ell}} = \frac{1/2}{1 - \frac{\ell}{n+1}}.$$

Then from $r_{\ell,n+h} \leq 2^{-h}/(1 - k/n)^h$ for $\ell \leq k$,

$$P_{k,n+h} = \sum_{\ell=0}^k p_{\ell,n+h} = \sum_{\ell=0}^k p_{\ell,n} \prod_{g=1}^h r_{\ell,n+g} \leq \sum_{\ell=0}^k p_{\ell,n} \cdot 2^{-h} \cdot (1 - k/n)^{-h} = P_{k,n} \cdot 2^{-h} \cdot (1 - k/n)^{-h}.$$

□

Lemma A.3. Again let $\Phi_{k,n}$ denote the usual normal approximation to the binomial probability $P_{k,n}$. Let $c > 0$ be fixed and let $n_0(c, k)$ be the smallest real value satisfying

$$\Phi_{k,n_0} \leq \frac{c}{k}, \quad n_0 > 2k.$$

Then with $0 < c' < c$ fixed, for some $C(c, c')$ made explicit below,

$$\lim_{k_0 \rightarrow \infty} \sup_{k \geq k_0} |n_0(c, k) - n_0(c', k)| / \sqrt{n_0(c, k)} \leq C.$$

Proof. Now

$$\Phi_{k,n} = \Phi\left(\frac{2k-n}{\sqrt{n}}\right).$$

Let $z(c, k) = \Phi^{-1}\left(\frac{c}{k}\right)$. Then n_0 solves,

$$\frac{2k-n_0}{\sqrt{n_0}} = z(c, k),$$

and then $n_0 = 2k - z\sqrt{n_0}$ and so $\sqrt{n_0} = (\sqrt{8k + z^2} - z)/2$. Now as $k \rightarrow \infty$, $z(c, k) = \Phi^{-1}\left(\frac{c}{k}\right) = -\sqrt{2\log(k)}(1 + o(1))$ tends to infinity, in such a way that to leading order it doesn't depend on c . We can say more. Suppose we wish to compare $z(c', k)$ with $z(c, k)$ precisely for large k , where $c' < c$ are both fixed. This is the same thing as comparing $\Phi^{-1}(\alpha)$ with $\Phi^{-1}\left(\frac{c'}{c}\alpha\right)$ for small α . Consider the difference of these two quantities,

$$\Psi(\beta; \alpha) = \Phi^{-1}(\alpha) - \Phi^{-1}((1-\beta)\alpha),$$

where we introduce $\beta = 1 - c'/c \in (0, 1)$.

We compare this to the β -quantile of the conditional distribution of the random variable $Y = z_\alpha - Z$, where $Z \sim N(0, 1)$ and Y is conditioned on $Z < z_\alpha$, where $z_\alpha \equiv \Phi^{-1}(\alpha)$. The density of the random variable Y has the exact form $f(y; \alpha) \propto \exp(-y(|z_\alpha| + y/2))$ on $y \geq 0$. Each member of this family of densities is less dispersed than the half-normal density $\propto e^{-y^2/2}$ on $y > 0$. Let $F^{-1}(\beta; \alpha)$ denote the β -th quantile of $f(y; \alpha)$. This stays in a bounded set as $\alpha \rightarrow 0$:

$$\sup_{0 < \alpha < 1/2} F^{-1}(\beta; \alpha) \leq \Phi^{-1}(1/2 + \beta/2), \quad 0 \leq \beta \leq 1.$$

In terms of this quantile, we have the identity

$$\Psi(\beta; \alpha) = F^{-1}(\beta; \alpha).$$

Hence

$$\sup_{\alpha < c/k_0} |\Psi(1 - \frac{c'}{c}; \alpha)| < \Phi^{-1}\left(1 - \frac{c'}{2c}\right),$$

The function $G(z; k) \equiv (\sqrt{8k + z^2} - z)/2$ obeys $\frac{\partial}{\partial z} G(z) \leq C_1$. Since

$$n_0(c, k) = [G(z(c, k); k)]^2$$

we have

$$\begin{aligned} |n_0(c, k) - n_0(c', k)| &\leq 2G(z(c, k); k)|G(z(c, k); k) - G(z(c', k); k)| + (G(z(c, k); k) - G(z(c', k); k))^2 \\ &\leq 2 \cdot G(z(c, k); k) \cdot C_1 |z(c, k) - z(c', k)| + C_1^2 \cdot |z(c, k) - z(c', k)|^2 \\ &= 2 \cdot G(z(c, k); k) \cdot C_1 \cdot \Phi^{-1}\left(1 - \frac{c'}{2c}\right) + C_1^2 \cdot \Phi^{-1}\left(1 - \frac{c'}{2c}\right)^2 \end{aligned}$$

Hence for large k ,

$$|n_0(c, k) - n_0(c', k)|/\sqrt{n_0(c, k)} \leq C_2(c, c'),$$

where $C_2(c', c) \equiv 1 + 2 \cdot C_1 \cdot \Phi^{-1}\left(1 - \frac{c'}{2c}\right)$ and we are assuming $c' < c$. □

We combine these as follows.

Lemma A.4. Fix $\delta \in (1/2, 1)$ and consider a sequence of tuples (m, M) with $M \rightarrow \infty$, and $m \sim \delta M$; and set $k \equiv M - m$. Let $\nu_k \equiv \frac{.26}{k} + e^{-\sqrt{k}}$ denote the error term in (11). Let $n_1 = n_1(q^*, k, M)$ solve

$$\Phi_{k, n_1} = \frac{\log(1/q^*)}{M} + \nu_k.$$

Let $c = \log(1/q^*) \cdot (1 - \delta)$. For all sufficiently large k ,

$$n_0(c + 0.27, k) > n_1(q^*, k, M) > n_0(c, k). \quad (13)$$

Let $n_2(q^*, k, M)$ denote the smallest integer solving

$$P_{k, n_2} \leq \frac{\log(1/q^*)}{M}.$$

Then for k_0 sufficiently large, there is an $h = h(c, k_0) > 0$ fixed independently of $k > k_0$ so that

$$n_1 \leq n_2 \leq n_1 + h. \quad (14)$$

Proof. We earlier gave the formula $n_0(c, k) = [(\sqrt{8k + z_0^2} - z_0)/2]^2$, in terms of k and $z_0 = \Phi^{-1}(c/k)$. By inspection, n_0 is monotone decreasing in z_0 . Similarly, we have:

$$n_1 = [(\sqrt{8k + z_1^2} - z_1)/2]^2, \quad z_1 = \Phi^{-1}\left(\frac{\log(1/q^*)}{M} + \nu_k\right).$$

Again n_1 is monotone decreasing in z_1 . Now we observe that for large k , $.26/k + \exp(-\sqrt{k}) < .27/k$. For such k ,

$$z_0(c, k) \geq z_1(q^*, M, k) \geq z_0(c + 0.27, k),$$

and (13) follows.

Now note that by (11)

$$\frac{\log(1/q^*)}{M} = \Phi_{k, n_1} - \nu_k \leq P_{k, n_1} \leq \Phi_{k, n_1} + \nu_k = \frac{\log(1/q^*)}{M} \cdot (1 + M \cdot \nu_k / \log(1/q^*)). \quad (15)$$

Now from $2k = n_1 + z_1\sqrt{n_1}$, we have $(1 - \frac{k}{n_1}) = \frac{1}{2} + \frac{|z_1|}{2\sqrt{n_1}}$. Hence $2^{-h}(1 - k/n_1)^{-h} = (1 + |z_1|/\sqrt{n_1})^{-h}$. Picking $h > 2$ a positive constant, and taking into account that $M\nu_k = O(k \exp(-\sqrt{k})) = O(1/k)$ while $|z_1|/\sqrt{n_1} > 1/\sqrt{k}$ (say) for large k , we get that along our sequence $k \sim (1 - \delta)M$, we have for all sufficiently large k_0 (say) that

$$\begin{aligned} (1 + |z_1|/\sqrt{n_1})^{-h} \cdot (1 + M \cdot \nu_k / \log(1/q^*)) &\leq (1 + k^{-1/2})^{-1} \cdot (1 + o(k^{-1/2})) \\ &< 1, \quad k > k_0. \end{aligned}$$

Applying (12) and (15), we have for $k > k_0$:

$$P_{k, n_1+h} < \frac{\log(1/q^*)}{M} \leq P_{k, n_1}.$$

It follows that $n_1 \leq n_2 \leq n_1 + h$. □

We apply these lemmas to our problem, in which $\delta \in (1/2, 1)$, $m \sim \delta M$ with $M \rightarrow \infty$. Setting $\ell_+ = M - n_2(q^*, M - m, M)$ yields

$$P_{M-m, M-\ell_+} \leq \frac{\log(1/q^*)}{M},$$

and that ℓ_+ is the largest value of ℓ with this property. For $c = \log(1/q^*) \cdot (1 - \delta)$, the previous lemma gives

$$M - n_0(c, M - m) \geq M - n_2 \geq M - (n_0(c + 0.27, M - m) + h),$$

while Lemma A.3 implies that the two sides differ by at most a term $\Delta(c, m, M) = C(c, c + 0.27)\sqrt{n_0(c, M - m)} + h(c, k_0)$. We immediately obtain that $|\ell_{\pm} - (M - n_0)| \leq \Delta(c, m, M)$, and of course by our definitions, $|\ell^* - \ell_+| \leq 1$.

Finally, the identities $2k = n_0 + z_0\sqrt{n_0}$ and $\sqrt{n_0} = (\sqrt{8k + z_0^2} - z_0)/2$ yield

$$\begin{aligned} n_0(c, k) &= 2k - (\sqrt{8k + z_0^2} - z_0)/2 \cdot z_0(c, k) \\ &\sim 2k + 2\sqrt{k \log(k)} \cdot (1 + o(1)) \\ &= 2k + 2\sqrt{k} \cdot \sqrt{\log(M)} \cdot (1 + o(1)). \end{aligned}$$

Combining the above formulas,

$$\begin{aligned}
\epsilon_{mb}^*(m, M, B; [0, 1]) &= \ell^*/M = (M - n_0)/M + O(\Delta/M) \\
&= (M - 2k)/M - \frac{\sqrt{2k}}{\sqrt{M}} \cdot \frac{\sqrt{2\log(M)}}{\sqrt{M}}(1 + o(1)) + O(\Delta/M) \\
&= (M - 2(M - m))/M - \frac{\sqrt{2(M - m)}}{\sqrt{M}} \cdot \frac{\sqrt{2\log(M)}}{\sqrt{M}}(1 + o(1)) + O(\Delta/M) \\
&= (2\delta - 1) - \sqrt{2(1 - \delta)} \cdot \frac{\sqrt{2\log(M)}}{\sqrt{M}} + o(\gamma) \\
&= \epsilon_{sb}^*(m, M; [0, 1]) - \sqrt{2(1 - \delta)} \cdot \gamma + o(\gamma),
\end{aligned}$$

where we used $O(\Delta/M) = o(\gamma)$.

B First Proof of Theorem 3.1

The proof of Theorem 3.1 relies on three lemmas.

Lemma B.1. (Rank-deficient matrix) *Consider the rank-deficient $n \times N$ ($n < N$) measurement matrix G with $\text{rank}(G) = r < n$ and $x_0 \in \mathbf{R}^N$ generating measurements $b = Gx_0$. The minimum- ℓ_1 optimization problem*

$$\min \|x\|_1 \quad \text{subject to} \quad Gx = b$$

has the same solution set as the reduced-dimensional problem

$$\min \|x\|_1 \quad \text{subject to} \quad Ax = y,$$

where A is a full-row-rank matrix of size $r \times N$ and $y = Ax_0$.

Proof. Using the SVD $G = U\Sigma V^T$, where $U \in \mathbf{R}^{n \times r}$, $V \in \mathbf{R}^{N \times r}$, and $\Sigma \in \mathbf{R}^{r \times r}$. Then

$$\begin{aligned}
Gx &= b, \\
\Sigma^{-1}U^T Gx &= \Sigma^{-1}U^T b, \\
V^T x &= \Sigma^{-1}U^T b.
\end{aligned}$$

Setting $A = V^T$ and $y = \Sigma^{-1}U^T b$ completes the proof. \square

Lemma B.2. (Block structure of Gram matrix of anisotropically undersampled FT) *Consider a d -dimensional complex-valued array x defined on a Cartesian grid of size $N = T_0 \times T_1 \times T_2 \times \dots \times T_{d-1}$. Let $\mathcal{D} = \{0, 1, 2, \dots, d-1\}$ denote the possible indices of the different underlying Cartesian axes. Further, let $\mathcal{E} \subset \mathcal{D}$ denote the indices of axes along which exhaustive samples are taken, and $\mathcal{P} = \mathcal{D} \setminus \mathcal{E}$, the remaining indices which are sampled partially. Then $\mathcal{D} = \mathcal{E} \cup \mathcal{P}$ and, with $d_{\mathcal{E}} = \#\mathcal{E}$ exhaustively sampled dimensions and $d_{\mathcal{P}} = \#\mathcal{P}$ partially sampled dimensions, $d = d_{\mathcal{E}} + d_{\mathcal{P}}$. Let the end-to-end measurement operator be represented by the $n \times N$ complex-valued matrix A . Then, the complex Hermitian Gram matrix $G = A^*A \in \mathbf{C}^{N \times N}$ is block-diagonal with $\prod_{j \in \mathcal{E}} T_j$ identical blocks each of size $\prod_{j \in \mathcal{P}} T_j$.*

*The corresponding result for real-valued A and real-valued symmetric A^*A also holds.*

Proof. Let $\mathcal{K} \subset \mathbf{R}^d$ denote the set of all tuples $k = (k_0, \dots, k_{d-1})$ that get sampled. Let e_j denote the j -th standard unit basis vector, $j = 0, \dots, d-1$, let $V_{\mathcal{E}} \subset \mathbf{R}^d$ denote the linear span of $\{e_j, j \in \mathcal{E}\}$, let $\mathcal{K}_{\mathcal{E}} = \text{Proj}_{V_{\mathcal{E}}} \mathcal{K}$ denote the orthogonal projection of the sampled tuples on the (span of the) exhaustively sampled dimensions. Correspondingly let $V_{\mathcal{P}} \subset \mathbf{R}^d$ denote the linear span of $\{e_j, j \in \mathcal{P}\}$, let $\mathcal{K}_{\mathcal{P}} = \text{Proj}_{V_{\mathcal{P}}} \mathcal{K}$ denote the projection of the sampled tuples on the (span of the) partially sampled dimensions. Then $\mathcal{K}_{\mathcal{E}}$ is, speaking informally, a Cartesian product of intervals. Formally, for each index of an exhaustively sampled dimension $j \in \mathcal{E}$, let $\mathcal{K}_j = \{0, \dots, T_j - 1\}$ denote the full range of that index. Then $\mathcal{K}_{\mathcal{E}}$ is an orthogonal sum $\mathcal{K}_{\mathcal{E}} = \bigoplus_{j \in \mathcal{E}} \mathcal{K}_j \cdot e_j$ and \mathcal{K} itself is an orthogonal sum

$$\mathcal{K} = \mathcal{K}_{\mathcal{P}} \bigoplus \mathcal{K}_{\mathcal{E}},$$

Informally, \mathcal{K} is an ‘irregular’ set of indices $\mathcal{K}_{\mathcal{P}}$ ‘times’ a Cartesian product $\mathcal{K}_{\mathcal{E}}$, and its cardinality obeys the product formula: $\#\mathcal{K} = \#\mathcal{K}_{\mathcal{P}} \times \#\mathcal{K}_{\mathcal{E}}$. A certain multiplicative relation generalizes the product formula. For each tuple $k \in \mathcal{K}$, let $k_{\mathcal{P}}$ denote the projection $Proj_{V_{\mathcal{P}}} k$ and similarly let $k_{\mathcal{E}} = Proj_{V_{\mathcal{E}}} k$. For an expression $c(k)$ obeying the factorization $c(k) = a(k_{\mathcal{E}})b(k_{\mathcal{P}})$, we have

$$\sum_{k \in \mathcal{K}} c(k) = \sum_{k \in \mathcal{K}} a(k_{\mathcal{E}})b(k_{\mathcal{P}}) = \left[\sum_{k_{\mathcal{E}} \in \mathcal{K}_{\mathcal{E}}} a(k_{\mathcal{E}}) \right] \cdot \sum_{k_{\mathcal{P}} \in \mathcal{K}_{\mathcal{P}}} b(k_{\mathcal{P}}). \quad (16)$$

The (k, t) element of the Fourier matrix can be written

$$F_k(t) = \frac{1}{\sqrt{N}} \exp \left\{ 2\pi i \left(\sum_{j=0}^{d-1} k_j t_j / T_j \right) \right\},$$

where $t = (t_0, \dots, t_{d-1})$, and $k = (k_0, \dots, k_{d-1})$. The inner product between two distinct columns u and t of A is thus given by

$$\begin{aligned} G_{t,u} &= (A^* A)_{t,u} = \sum_{k \in \mathcal{K}} F_k(t) F_k^*(u) \\ &= \frac{1}{N} \sum_{k \in \mathcal{K}} \exp \left(2\pi i \sum_{j \in \mathcal{D}} k_j (t_j - u_j) / T_j \right) \\ &= \frac{1}{N} \sum_{k \in \mathcal{K}} \exp \left(2\pi i \cdot \left[\sum_{j \in \mathcal{P}} k_j (t_j - u_j) / T_j + \sum_{j \in \mathcal{E}} k_j (t_j - u_j) / T_j \right] \right) \\ &= \frac{1}{\prod_{j \in \mathcal{P}} T_j} \sum_{t \in \mathcal{T}} \exp \left(2\pi i \sum_{j \in \mathcal{P}} k_j (t_j - u_j) / T_j \right) \times \left[\frac{1}{\prod_{j \in \mathcal{E}} T_j} \exp \left(2\pi i \sum_{j \in \mathcal{E}} k_j (t_j - u_j) / T_j \right) \right] \\ &= \frac{1}{\prod_{j \in \mathcal{P}} T_j} \sum_{k \in \mathcal{K}_{\mathcal{P}}} \exp \left(2\pi i \sum_{j \in \mathcal{P}} k_j (t_j - u_j) / T_j \right) \times \left[\frac{1}{\prod_{j \in \mathcal{E}} T_j} \sum_{t \in \mathcal{T}_{\mathcal{E}}} \exp \left(2\pi i \sum_{j \in \mathcal{E}} k_j (t_j - u_j) / T_j \right) \right] \end{aligned}$$

where we used $N = \prod_{j \in \mathcal{E}} T_j \cdot \prod_{j \in \mathcal{P}} T_j$ as well as the multiplicative relation (16) for the multiplicative expression $c(k) = \exp \left(2\pi i \sum_{j \in \mathcal{D}} k_j (t_j - u_j) / T_j \right) = a(k_{\mathcal{E}})b(k_{\mathcal{P}})$ with $a(k_{\mathcal{E}}) = \exp \left(2\pi i \sum_{j \in \mathcal{E}} k_j (t_j - u_j) / T_j \right)$ and $b(k_{\mathcal{P}}) = \exp \left(2\pi i \sum_{j \in \mathcal{P}} k_j (t_j - u_j) / T_j \right)$. Recall the Dirichlet sum formula: for an integer $u \in \{0, 1, \dots, T-1\}$,

$$\sum_{k=0}^{T-1} \exp \left(\frac{2\pi u}{T} k i \right) = \begin{cases} T & u = 0 \\ 0 & u \neq 0 \end{cases}.$$

Apply this to each exhaustively-sampled coordinate $j \in \mathcal{E}$, obtaining:

$$\frac{1}{T_j} \sum_{\mathcal{K}_j} \exp (2\pi i k_j (t_j - u_j) / T_j) = \delta(t_j - u_j), \quad j \in \mathcal{E},$$

where $\delta()$ denotes the usual Kronecker symbol. We have

$$G_{t,u} = \frac{1}{\prod_{j \in \mathcal{P}} T_j} \sum_{k \in \mathcal{K}_{\mathcal{P}}} \exp \left(2\pi i \sum_{j \in \mathcal{P}} k_j (t_j - u_j) / T_j \right) \times \prod_{j \in \mathcal{E}} \delta(t_j - u_j). \quad (17)$$

We see that $G_{t,u} = 0$ unless $t_j = u_j$ for all $j \in \mathcal{E}$. This indeed is the advertised block structure. \square

Lemma B.3. (Singular vectors of the Gram matrix) Consider the Gram matrix $G = A^*A$ in a special case of Lemma B.2, where $d = 2$ and $\mathcal{E} = \{0\}$, $\mathcal{P} = \{1\}$, so A implements anisotropic undersampling of the 2D Fourier transform on $T_0 \times T_1$ arrays. Namely, assume that the Fourier transform is followed by selection of columns $k_{1,i}$, $0 \leq k_{1,i} < T_1$ with exhaustive sampling of all entries $\{(k_0, k_{1,i}) : 0 \leq k_0 < T_0\}$ in each selected column. Necessarily $i = 1, \dots, M \equiv n/T_0$. By Lemma B.2, G is block-diagonal with T_0 identical blocks of size $T_1 \times T_1$. Let $G^{(1)}$ represent the upper left diagonal such $T_1 \times T_1$ block. Then, $\text{rank}(G^{(1)}) = M$ and the M principal eigenvectors of the T_1 by T_1 matrix $G^{(1)}$ are given by:

$$V_\ell = (1, w_\ell, w_\ell^2, \dots, w_\ell^{T_1-1}), \quad \ell \in \mathcal{K}_1,$$

where $w_\ell = \exp(2\pi i \ell / T_1)$ and $\mathcal{K}_1 = (k_{1,i})_{i=1}^M$ denotes the collection of all sampled column indices.

Proof. We prove that for $\ell \in \mathcal{K}_1$, V_ℓ is an eigenvector by verifying $\sum_{\ell=0}^{N-1} G^{(1)}(t, u) V_\ell(u) = \lambda_\ell V_\ell(t)$, in fact by showing that $\lambda_\ell = 1$. Lemma B.2 – specifically (17) – gives us that for $k = (k_0, k_1)$ and

$$G_{t,u} = \left(\frac{1}{\prod_{j \in \mathcal{P}} T_j} \sum_{k \in \mathcal{K}_{\mathcal{P}}} \exp(2\pi i \cdot \sum_{j \in \mathcal{P}} k_j (t_j - u_j) / T_j) \right) \cdot \prod_{j \in \mathcal{E}} \delta(t_j - u_j).$$

Because $d = 2$ and k_0 is sampled exhaustively, the upper left $T_1 \times T_1$ block has the form:

$$G_{(0,t),(0,u)} = \frac{1}{T_1} \sum_{k \in \mathcal{K}_1} \exp(2\pi i k(t - u) / T_1), \quad (t, u) \in \{0, \dots, T_1 - 1\}^2,$$

where now k, t , and u are integers. The matrix $G^{(1)}$ has entries $G^{(1)}(t, u) \equiv G_{(0,t),(0,u)}$ for $0 \leq t, u < T_1$. It has rank $M = \#\mathcal{T}_1$ by inspection of the preceding display.

$$\begin{aligned} \sum_{u=0}^{T_1-1} G^{(1)}(t, u) V_\ell(u) &= \sum_{u=0}^{T_1-1} \left(\frac{1}{T_1} \sum_{k \in \mathcal{K}_1} \exp(2\pi i k(t - u) / T_1) \right) \exp(2\pi i u \ell / T_1) \\ &= \sum_{k \in \mathcal{K}_1} \left(\frac{1}{T_1} \exp(2\pi i k t / T_1) \right) \left(\sum_{u=0}^{T_1-1} \exp(2\pi i u(k - \ell) / T_1) \right) \\ &= \sum_{k \in \mathcal{K}_1} \left(\frac{1}{T_1} \exp(2\pi i k t / T_1) \right) (T_1 \delta(k - \ell)) \\ &= \exp(2\pi i \ell t / T_1) = V_\ell(t). \end{aligned}$$

□

Proof of Theorem 3.1. Consider the two convex optimization problems

$$(P_1) \quad \min \|x\|_{1, \mathbb{C}^N} \quad \text{subject to} \quad Ax = y,$$

$$(P_2) \quad \min \|x\|_{1, \mathbb{C}^N} \quad \text{subject to} \quad A^*Ax = A^*y,$$

where A is an $n \times N$ ($n < N$) matrix having n nonzero singular values (i.e., A has full row rank). Problem (P_1) is equivalent to (P_2) because A^* has full column rank n ; hence their solution sets match. By Lemma B.2, $G = A^*A$ is block-diagonal. By separability of ℓ_1 minimization, we can solve the T_0 block subproblems each of size $T_1 \times T_1$ individually. Because blocks are identical and $\text{rank}(G) = \lfloor \delta T_1 \rfloor T_1$, $\text{rank}(G^b) = \lfloor \delta T_1 \rfloor$ for blocks $b = 1, \dots, N$. By Lemma B.1, we know that we can solve equivalent full-row-rank problems of size $\lfloor \delta T_1 \rfloor \times T_1$ as long as we find the right singular vectors. By Lemma B.3 we know that right singular vectors are defined by the partial Fourier matrix. □

C Second Proof of Theorem 3.1

We begin with terminology. For an array $x = (x(t_0, t_1), 0 \leq t_i \leq m_i)$, we call the collection of entries $x(\cdot, t_1)$ a *row* and a collection $x(t_0, \cdot)$ a *column*. This is consistent with our depiction in Figure 3 of the main paper.

Let $V_{c;m_0,m_1}$ denote the *vec* operation taking arrays in $\mathbf{C}^{m_0 \times m_1}$ into vectors $\mathbf{C}^{m_0 \cdot m_1}$ in *column-major* order;

$$(V_{c;m_0,m_1}x)(i_0 \cdot m_0 + i_1) = x(i_0, i_1), \quad 0 \leq i_0 < m_0; 0 \leq i_1 < m_1.$$

Thus $(V_{c;m_0,m_1}x)(0) = x(0, 0)$, $(V_{c;m_0,m_1}x)(1) = x(0, 1)$, $(V_{c;m_0,m_1}x)(2) = x(0, 2)$, etc.

In the first half of the proof we will need $V_{c;M,M}$ exclusively and denote this simply V for short. Of course V is an ℓ_2 isometry which is also an ℓ_1 isometry:

$$\begin{aligned} \|x\|_{2,\mathbf{C}^{M^2}} &= \|V(x)\|_{2,\mathbf{C}^{M \times M}}, \\ \|x\|_{1,\mathbf{C}^{M^2}} &= \|V(x)\|_{1,\mathbf{C}^{M \times M}}. \end{aligned}$$

Lemma C.1. *There is an ℓ_2 isometry T from $\mathbf{C}^{M^m} \mapsto \mathbf{C}^{M \times m}$ so that*

$$T \circ A \circ V = \mathcal{F}_{\text{AUS}}. \quad (18)$$

Proof. We explicitly construct the isomorphism T in (18). Let $\mathcal{F}_c \equiv \mathcal{F}_{c;m_0,m_1}$ denote the operator on $m_0 \times m_1$ arrays that applies the 1D discrete Fourier transform to each *column* separately, returning an $m_0 \times m_1$ array. Let $\mathcal{F}_r \equiv \mathcal{F}_{r;m_0,m_1}$ denote the operator on $m_0 \times m_1$ arrays that applies the 1D discrete Fourier transform to each *row* separately, returning an $m_0 \times m_1$ array.

It is well-known that the 2D Discrete Fourier transform on $M \times M$ arrays has the factorization

$$\mathcal{F}_2 = \mathcal{F}_r \mathcal{F}_c = \mathcal{F}_{r;M,M} \mathcal{F}_{c;M,M},$$

the 1D Fourier transform of columns followed by the 1D Fourier transform of rows. Let \mathcal{K} denote a collection of m row indices $0 \leq k_i < M$ and let $\mathcal{S}_{r,\mathcal{K}}$ denote the operator from $M \times M$ arrays to $M \times m$ arrays that simply selects those rows with indices in \mathcal{K} . We observe the identity

$$\mathcal{S}_{r,\mathcal{K}} \mathcal{F}_{r;M,M} = \mathcal{F}_{r;M,m} \mathcal{S}_{r,\mathcal{K}}. \quad (19)$$

In words, we can either first 1D Fourier transform each row individually, and then select certain rows, or else we can select those same rows and then Fourier transform them; either way we get the same outcome. Note that the two Fourier transform operators in this relation have different domains; one operates on $M \times m$ arrays and one operates on $M \times M$ arrays.

Our anisotropic undersampling operator has been defined by:

$$\mathcal{F}_{\text{AUS}} = \mathcal{S}_{r,\mathcal{K}} \mathcal{F}_2.$$

Based on the previous paragraph, we can equivalently write

$$\mathcal{F}_{\text{AUS}} = \mathcal{F}_r \mathcal{S}_{r,\mathcal{K}} \mathcal{F}_c = \mathcal{F}_{r;M,m} \mathcal{S}_{r,\mathcal{K}} \mathcal{F}_{c;M,M}. \quad (20)$$

Let now $V_{c;M,m}$ be a *vec* operator that maps from $M \times m$ arrays to $M \cdot m$ vectors, again by vectorizing in *column-major* order; namely,

$$V_{c;M,m}(y)(i_0 M + i_1) = y(i_0, i_1) \quad 0 \leq i_0, i_1 < M.$$

Thus $(V_{c;M,m}y)(0) = y(0, 0)$, $(V_{c;M,m}y)(1) = y(0, 1)$, $(V_{c;M,m}y)(2) = y(0, 2)$, etc. Then of course $V_{c;M,m}$ is an isometry between $\mathbf{C}^{M \times M}$ and $\mathbf{C}^{M \cdot m}$, and so one-one.

From now on the operator $V_{c;M,m}$ previously denoted V , will always be spelled out as $V_{c;M,m}$, to keep domains and ranges unambiguous.

Now define $T : \mathbf{C}^{M^m} \mapsto \mathbf{C}^{M \times m}$ by

$$T = \mathcal{F}_{r;M,m} V_{c;M,m}^{-1}. \quad (21)$$

In words, T builds an $M \times m$ array and then applies the 1D Fourier transform to each resulting row. We now make the key observation:

$$A = V_{c;M,m} \mathcal{S}_{r,\mathcal{K}} \mathcal{F}_c V_{c;M,M}^{-1}. \quad (22)$$

To check this, note first that the domain is indeed \mathbf{C}^{M^2} and the range is indeed $\mathbf{C}^{M \cdot m}$. We previously defined A as a block diagonal operator $I_M \otimes A^{(1)}$, where $A^{(1)} : \mathbf{C}^M \mapsto \mathbf{C}^m$ is the pipeline $A^{(1)} = \mathcal{S}_{1,\mathcal{K}} \mathcal{F}_1$ of two operators:

\mathcal{F}_1 , a 1D Fourier transform of M -vectors followed by $\mathcal{S}_{1,\mathcal{K}}$ a selection of certain elements out of those M vectors. Checking definitions we see that

$$\mathcal{S}_{r,\mathcal{K}} = V_{c;M,m}^{-1}(I_M \otimes \mathcal{S}_{1,\mathcal{K}})V_{c;M,M}$$

and

$$\mathcal{F}_{c;M,M} = V_{c;M,m}^{-1}(I_M \otimes \mathcal{F}_1)V_{c;M,M}.$$

Hence

$$\begin{aligned} V_{c;M,m}\mathcal{S}_{r,\mathcal{K}}\mathcal{F}_cV_{c;M,M}^{-1} &= V_{c;M,m}\left(V_{c;M,m}^{-1}(I_M \otimes \mathcal{S}_{1,\mathcal{K}})V_{c;M,M}\right)\left(V_{c;M,m}^{-1}(I_M \otimes \mathcal{F}_1)V_{c;M,M}\right)V_{c;M,M}^{-1} \\ &= (I_M \otimes \mathcal{S}_{1,\mathcal{K}})(I_M \otimes \mathcal{F}_1) \\ &= I_M \otimes (\mathcal{S}_{1,\mathcal{K}}\mathcal{F}_1) \\ &= I_M \otimes A^{(1)} \\ &= A, \end{aligned}$$

which proves (22).

We now verify (18)

$$\begin{aligned} \mathcal{F}_{\text{AUS}} &= \mathcal{S}_{r;\mathcal{K}}\mathcal{F}_2 \\ &= \mathcal{S}_{r;\mathcal{K}}\mathcal{F}_{r;M,M}\mathcal{F}_{c;M,M} \\ &= \mathcal{F}_{r;M,m}\mathcal{S}_{r;\mathcal{K}}\mathcal{F}_{c;M,M} \quad \text{by (19) - (20)} \\ &= \left(\mathcal{F}_{r;M,m}V_{c;M,m}^{-1}\right)\left(V_{c;M,m}\mathcal{S}_{r;\mathcal{K}}\mathcal{F}_{c;M,M}V_{c;M,M}^{-1}\right)V_{c;M,M} \\ &= TAV_{c;M,M} \quad \text{by (21) - (22)} \end{aligned}$$

where, as remarked earlier, both T and V are both isometries. \square

We now use the representation $\mathcal{F}_{\text{AUS}} = TAV$ to prove our main result.

Proof. (of Theorem 3.1)

Fix x_0 , generating undersampled measurements $\hat{x}_{\text{AUS}} = \mathcal{F}_{\text{AUS}}(x_0)$. Consider the instance of (P_{AUS}) based on measurements vector \hat{x}_{AUS} . Let x_1 denote some specific solution of (P_{AUS}) . As a solution, it must obey the feasibility condition

$$\mathcal{F}_{\text{AUS}}(x_1) = \mathcal{F}_{\text{AUS}}(x_0).$$

Let $\mathbf{x}_0 = V(x_0)$ and $\mathbf{y}_0 = A\mathbf{x}_0$ and consider $\mathbf{x}_1 = V(x_1)$ as a candidate solution for $(P_{1,\mathcal{C}})$ with data \mathbf{y}_0 . We need to check that \mathbf{x}_1 is feasible for $(P_{1,\mathcal{C}})$ i.e. that $\mathbf{y}_0 = A\mathbf{x}_1$.

$$\begin{aligned} \mathbf{y}_0 &= A\mathbf{x}_0 \\ &= AV(x_0) \\ &= T^{-1}\mathcal{F}_{\text{AUS}}(x_0) \\ &= T^{-1}\mathcal{F}_{\text{AUS}}(x_1) \\ &= AV(x_1) \\ &= A\mathbf{x}_1. \end{aligned}$$

So \mathbf{x}_1 is indeed feasible for $(P_{1,\mathcal{C}})$. It follows that

$$\text{val}(P_{1,\mathcal{C}}) \leq \|\mathbf{x}_1\|_{1,\mathcal{C}M^2} = \|x_1\|_{1,\mathcal{C}M \times M} = \text{val}(P_{\text{AUS}}).$$

Arguing in the other direction, let \mathbf{x}_1 denote some solution of $(P_{1,\mathcal{C}})$. We consider $x_1 \equiv V^{-1}(\mathbf{x}_1)$ as a candidate solution of (P_{AUS}) . From the feasibility of \mathbf{x}_1 for $(P_{1,\mathcal{C}})$ we have $A\mathbf{x}_0 = A\mathbf{x}_1 = \mathbf{y}_1$, say. We check the feasibility

$$\mathcal{F}_{\text{AUS}}(x_1) = \mathcal{F}_{\text{AUS}}(x_0):$$

$$\begin{aligned} \mathcal{F}_{\text{AUS}}(x_0) &= TAV(x_0) \\ &= T\mathbf{y}_0 \\ &= T\mathbf{y}_1 \\ &= T\mathbf{A}\mathbf{x}_1 \\ &= TAV \cdot V^{-1}(\mathbf{x}_1) \\ &= TAVx_1 \\ &= \mathcal{F}_{\text{AUS}}(x_1). \end{aligned}$$

We conclude that

$$\text{val}(P_{1,\mathbf{C}}) \geq \text{val}(P_{\text{AUS}}).$$

Hence, $\text{val}(P_{1,\mathbf{C}}) = \text{val}(P_{\text{AUS}})$. So the two problems have identical optimal values and their solution sets are isomorphic under the vec mapping $V(\cdot)$. \square

D Proof of Theorem 7.1

For $\mathbf{X} = \mathbf{H}_d$, the arguments of Appendix B can all be redone, step-by-step, replacing the field \mathbf{C} by the hypercomplex algebra \mathbf{H}_d . The notation and basic pattern of argument are given in [38] and we won't repeat them. The basic idea is as follows. Let $n' = n/2^d$ and $N' = N/2^d$. The matrix A belongs to $\mathbf{H}_d^{n' \times n'}$, the matrix $G = A^\# A$ belongs to $\mathbf{H}_d^{N' \times N'}$ (here $\#$ denotes hypercomplex conjugation; again, see [38] for details). The hypercomplex entries $x(i)$ can be viewed as 2^d dimensional real vectors. The ℓ_1 norm can then be written:

$$\|\mathbf{x}\|_{1, H^d} = \sum_{i=1}^{N'} \|x(i)\|_{\ell_1^{2^d}(\mathbf{R})}.$$

The arguments of the preceding section go through without essential changes; the Dirichlet sum has this direct analog:

$$\sum_{t=0}^{T-1} \exp_{\mathbf{H}_d} \left(\frac{2\pi t}{T} u i \right) = \begin{cases} T & u = 0 \\ 0 & u \neq 0 \end{cases},$$

where $u \in \{0, \dots, T-1\}$, and $\exp_{\mathbf{H}_d}$ denotes the exponential function defined by the usual power series within the associative algebra \mathbf{H}_d . For other choices of \mathbf{X} , the theorem can be proved by realizing that the hypercomplex algebra \mathbf{H}_d is isomorphic to a subalgebra of the algebra of $2^d \times 2^d$ matrices with real entries. The reader is referred to [38, 35] for the details.

E Comparison to exponential bounds by Donoho and Tanner

Donoho and Tanner [16] give exponential bounds for the finite- N probability of successful reconstruction for the coefficient fields \mathbf{R}_+ and \mathbf{R} . They consider the following condition on ϵ at certain δ ,

$$0 \leq \epsilon \leq \epsilon_{\text{asy}}^*(\delta)(1 - R_\tau)$$

where R_τ is a certain multiplicative term having a real parameter $\tau \in (0, 1)$ which, by their bounds, implies

$$P\{\mathbf{x}_1 = \mathbf{x}_0\} \geq 1 - \tau.$$

Taking $\tau = 1/M$ and $m \sim \delta M$ we get:

$$\frac{\epsilon_{\text{asy}}^*(\delta) - \epsilon_{\text{sb}}^*(m, M)}{\epsilon_{\text{asy}}^*(\delta)} \leq R_{1/M}$$

where

$$R_{1/M} \simeq c \cdot \delta^{-1/2} \gamma_M$$

Figure 17 depicts the lower bounds on $\epsilon_{\text{sb}}^*(m, M)$ based on these bounds. In the case of real signals (cross-polytope), the formula obtained from the exponential bounds agrees, up to a proportionality constant, to our formula for η following this article's (3).

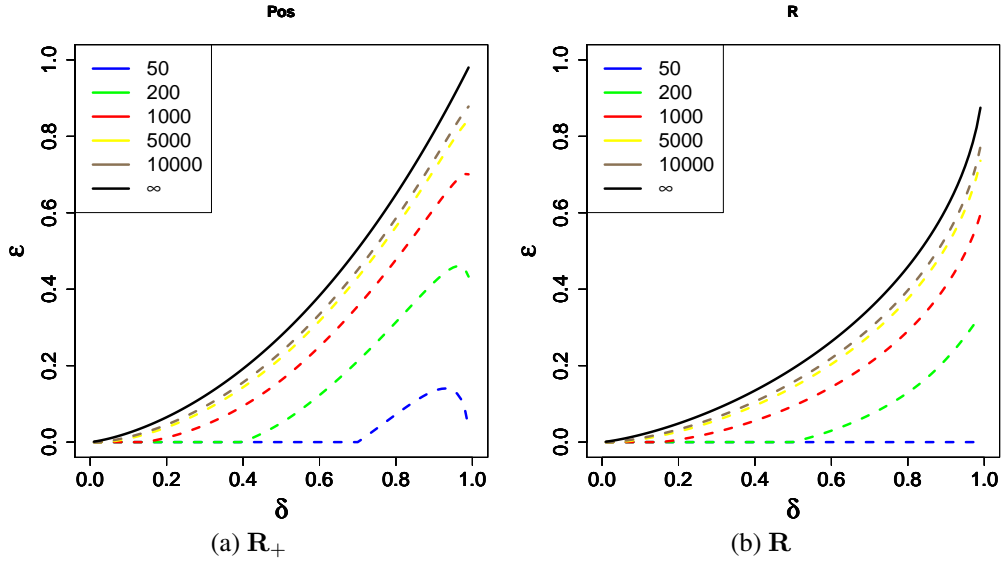


Figure 17: Lower bound on $\epsilon_{\text{sb}}^*(m, M)$ based on Donoho-Tanner exponential bounds. (left) Simplex (\mathbf{R}_+), and (right) Cross-polytope (\mathbf{R})

References

- [1] Mosek optimization software. Available online via <http://www.mosek.com>.
- [2] D. Amelunxen, M. Lotz, M. B. McCoy, and J. A. Tropp. Living on the edge: Phase transitions in convex programs with random data. *Information and Inference*, 3:224–294, 2014.
- [3] L. Applebaum, S. Howard, S. Searle, and R. Calderbank. Chirp sensing codes: Deterministic compressed sensing measurements for fast recovery. *Applied and Computational Harmonic Analysis*, 26(2):283–290, 2009.
- [4] E. J. Candès and T. Tao. Decoding by linear programming. *IEEE Trans. on Inform. Theory*, 51:4203–4215, 2005.
- [5] I. Y. Chun and B. Adcock. Uniform recovery from subgaussian multi-sensor measurements. *arXiv:1610.05758*, 2016.
- [6] D. L. Donoho. Neighborly polytopes and sparse solution of underdetermined linear equations. *Technical Report, Department of Statistics, Stanford University*, 2004.
- [7] D. L. Donoho. Compressed sensing. *IEEE Transactions on Information Theory*, 52:489–509, April 2006.
- [8] D. L. Donoho and Xiaoming Huo. Uncertainty principles and ideal atomic decomposition. *IEEE Trans. Inform. Theory*, 47(7):2845–2862, 2001.
- [9] D. L. Donoho, I. Johnstone, and A. Montanari. Accurate prediction of phase transitions in compressed sensing via a connection to minimax denoising. *IEEE Transactions on Information Theory*, 59(6):3396–3433, June 2013.

- [10] D. L. Donoho, A. Maleki, and A. Montanari. Message passing algorithms for compressed sensing. *PNAS*, 106:18914–18919, 2009.
- [11] D. L. Donoho and J. Tanner. Neighborliness of randomly-projected simplices in high dimensions. *PNAS*, 102(27):9452–9457, 2005.
- [12] D. L. Donoho and J. Tanner. Counting faces of randomly projected polytopes when the projection radically lowers dimension. *Journal of American Mathematical Society*, 22:1–53, 2009.
- [13] D. L. Donoho and J. Tanner. Counting faces of randomly-projected polytopes when the projection radically lowers dimension. *J. AMS*, 22:1–53, 2009.
- [14] D. L. Donoho and J. Tanner. Observed universality of phase transitions in high-dimensional geometry, with implications for modern data analysis and signal processing. *Phil. Trans. R. Soc.*, 367:4273–4293, 2009.
- [15] D. L. Donoho and J. Tanner. Counting the faces of randomly-projected hypercubes and orthants, with applications. *Discrete & Computational Geometry*, 43(3):522–541, 2010.
- [16] D. L. Donoho and J. Tanner. Exponential bounds implying construction of compressed sensing matrices, error-correcting codes and neighborly polytopes by random sampling. *IEEE Transactions on Information Theory*, 56(4), 2010.
- [17] Armin Eftekhari, Han Lun Yap, Christopher J. Rozell, and Michael B. Wakin. The restricted isometry property for random block diagonal matrices. *Applied and Computational Harmonic Analysis*, 38(1):1 – 31, 2015.
- [18] L. Feng, T. Benkert, K. T. Block, D. K. Sodickson, R. Otazo, and H. Chandarana. Compressed sensing for body MRI. *Journal of Magnetic Resonance Imaging*, 2016.
- [19] J. E. Fowler, S. Mun, and E. W. Tramel. Block-based compressed sensing of images and video. *Foundations and Trends in Signal Processing*, 4(4):297–416, 2012.
- [20] S. Friedland, Q. Li, and D. Schonfeld. Compressive sensing of sparse tensors. *IEEE Trans. Image Process.*, 23(10), October 2014.
- [21] M. Friedlander and M. Saunders. ASP: A set of Matlab functions for solving Basis Pursuit-type problems., 2010. Available online via <http://web.stanford.edu/group/SOL/software/asp/>.
- [22] M. Friedlander and M. Saunders. A dual active-set quadratic programming method for finding sparse least-squares solutions. *DRAFT Technical Report, Department of Computer Science, University of British Columbia*, July 30 2012. Available online via <http://web.stanford.edu/group/SOL/software/asp/bpdual.pdf>.
- [23] M. Grant and S. Boyd. CVX: Matlab software for disciplined convex programming, version 1.21, May 2010. Available online via <http://cvxr.com/cvx>.
- [24] A. Greiser and M. von Kienlin. Efficient k-space sampling by density-weighted phase-encoding. *Magnetic resonance in Medicine*, 50(6):1266–1275, 2003.
- [25] J. C. Hoch, M. W. Maciejewski, M. Mobli, A. D. Schuyler, and A. S. Stern. Nonuniform sampling and maximum entropy reconstruction in multidimensional NMR. *Accounts of chemical research*, 47(2):708–717, 2014.
- [26] S.D. Howard, A.R. Calderbank, and S.J. Searle. A fast reconstruction algorithm for deterministic compressive sensing using second order reed-muller codes. In *Information Sciences and Systems, 2008. CISS 2008. 42nd Annual Conference on*, IEEE Conference on Information, Science and Systems, pages 11–15. IEEE, March 2008.
- [27] Q. Li, D. Schonfeld, and S. Friedland. Generalized tensor compressive sensing. *IEEE International Conference on Multimedia & Expo*, 2013.
- [28] G. Lu. Block compressed sensing of natural images. *15th IEEE International Conference on Digital Signal Processing*, pages 403–406, 2007.

- [29] M. Lustig, D. L. Donoho, and J. M. Pauly. Sparse MRI: The application of compressed sensing for rapid MR imaging. *Magnetic Resonance in Medicine*, 58(6):1182–1195, 2007.
- [30] M. Lustig, D. L. Donoho, J. M. Santos, and J. M. Pauly. Compressed sensing MRI. *IEEE Signal Processing Magazine*, 72, 2008.
- [31] B. Madore, G. H. Glover, N. J. Pelc, et al. Unaliasing by fourier-encoding the overlaps using the temporal dimension (UNFOLD), applied to cardiac imaging and fMRI. *Magnetic Resonance in Medicine*, 42(5):813–828, 1999.
- [32] G. J. Marseille, R. De Beer, M. Fuderer, A. F. Mehlkopf, and D. Van Ormondt. Nonuniform phase-encode distributions for MRI scan time reduction. *Journal of Magnetic Resonance*, 111(1):70–75, 1996.
- [33] G. McGibney, M. R. Smith, S. T. Nichols, and A. Crawley. Quantitative evaluation of several partial Fourier reconstruction algorithms used in MRI. *Magnetic Resonance in Medicine*, 30(1):51–59, 1993.
- [34] M. Mobli, M. W. Maciejewski, A. D. Schuyler, A. S. Stern, and J. C. Hoch. Sparse sampling methods in multidimensional NMR. *Physical Chemistry Chemical Physics*, 14(31):10835–10843, 2012.
- [35] H. Monajemi. *Phase transitions in deterministic compressed sensing, with application to magnetic resonance spectroscopy*. PhD thesis, Stanford University, 2016. Available online at <https://purl.stanford.edu/gf738wr7593>. Accessed on Feb 28, 2018.
- [36] H. Monajemi and D. L. Donoho. Clusterjob, a automated system for reproducibility and hassle-free submission of computational jobs to clusters. 2015. Available online via <https://github.com/monajemi/clusterjob>.
- [37] H. Monajemi and D. L. Donoho. Code and data supplement to "Sparsity/undersampling tradeoffs in anisotropic undersampling, with applications in MR imaging/spectroscopy". *Stanford Digital Repository*, 2017. Available online via <https://purl.stanford.edu/th702qm4100>.
- [38] H. Monajemi, D. L. Donoho, J. C. Hoch, and A. D. Schuyler. Incoherence of partial-component sampling in multidimensional NMR. *arXiv:1702.01830*, 2017.
- [39] H. Monajemi, S. Jafarpour, M. Gavish, Stat 330/CME 362 Collaboration, and D. L. Donoho. Deterministic matrices matching the compressed sensing phase transitions of Gaussian random matrices. *PNAS*, 110(4):1181–1186, 2013.
- [40] S. Oymak and J. A. Tropp. Universality laws for randomized dimension reduction, with applications. *arXiv:1511.09433*, 2015.
- [41] K. P. Pruessmann, M. Weiger, M. B. Scheidegger, P. Boesiger, et al. SENSE: sensitivity encoding for fast MRI. *Magnetic Resonance in Medicine*, 42(5):952–962, 1999.
- [42] P. Schmieder, A. S. Stern, G. Wagner, and J. C. Hoch. Application of nonlinear sampling schemes to COSY-type spectra. *Journal of Biomolecular NMR*, 3(5):569–576, 1993.
- [43] P. Schmieder, A. S. Stern, G. Wagner, and J. C. Hoch. Improved resolution in triple-resonance spectra by nonlinear sampling in the constant-time domain. *Journal of Biomolecular NMR*, 4(4):483–490, 1994.
- [44] D. K. Sodickson and W. J. Manning. Simultaneous acquisition of spatial harmonics (SMASH): fast imaging with radiofrequency coil arrays. *Magnetic Resonance in Medicine*, 38(4):591–603, 1997.
- [45] J. I. Tamir, M. Uecker, W. Chen, P. Lai, M. T. Alley, S. S. Vasanawala, and M. Lustig. T2 shuffling: Sharp, multicontrast, volumetric fast spin-echo imaging. *Magnetic Resonance in Medicine*, 2016.
- [46] T. Tao. An uncertainty principle for cyclic groups of prime order. *Mathematical Research Letters*, 2(1), 2005.
- [47] J. A. Tropp and A. C. Gilbert. Signal recovery from random measurements via orthogonal matching pursuit. *IEEE Trans. Inform. Theory*, 53(12):4655–4666, 2007.

- [48] S. S. Vasawala, M. T. Alley, B. A. Hargreaves, R. A. Barth, J. M. Pauly, and M. Lustig. Improved pediatric MR imaging with compressed sensing. *Radiology*, 256(2):607–616, 2010.
- [49] T. Zhang, U. Yousaf, A. Hsiao, J. Y. Cheng, M. T. Alley, M. Lustig, J. M. Pauly, and S. S. Vasawala. Clinical performance of a free-breathing spatiotemporally accelerated 3-D time-resolved contrast-enhanced pediatric abdominal MR angiography. *Pediatric Radiology*, 45(11):1635–1643, 2015.
- [50] B. Zhao, J. P. Haldar, A. G. Christodoulou, and Z. Liang. Image reconstruction from highly undersampled (k, t) -space data with joint partial separability and sparsity constraints. *IEEE Transactions on Medical Imaging*, 31(9):1809–1820, 2012.